Martin Haardt, et. Al. “ESPRIT and Closed-Form 2-D Angle Estimation with Planar Arrays.”
2000 CRC Press LLC. <http://www.engnetbase.com>.

ESPRIT and Closed-Form 2-D Angle Estimation with Planar Arrays

Martin Haardt
Siemens AG
Mobile Radio Networks

Michael D. Zoltowski
Purdue University

Cherian P. Mathews
University of West Florida

Javier Ramos
Polytechnic University of Madrid

63.1 Introduction

Estimating the directions of arrival (DOAs) of propagating plane waves is a requirement in a variety of applications including radar, mobile communications, sonar, and seismology. Due to its simplicity and high-resolution capability, *ESPRIT (Estimation of Signal Parameters via Rotational Invariance Techniques)* [18] has become one of the most popular signal subspace-based DOA or spatial frequency estimation schemes. ESPRIT is explicitly premised on a point source model for the sources and is restricted to use with array geometries that exhibit so-called invariances [18]. However, this requirement is not very restrictive as many of the common array geometries used in practice exhibit these invariances, or their output may be transformed to effect these invariances.

ESPRIT may be viewed as a complement to the MUSIC algorithm, the forerunner of all signal subspace-based DOA methods, in that it is based on properties of the signal eigenvectors whereas MUSIC is based on properties of the noise eigenvectors. This chapter concentrates solely on the use of ESPRIT to estimate the DOAs of plane waves incident upon an antenna array. It should be noted, though, that ESPRIT may be used in the dual problem of estimating the frequencies of sinusoids embedded in a time series [18]. In this application, ESPRIT is more generally applicable than MUSIC as it can handle damped sinusoids and provides estimates of the damping factors as well as the constituent frequencies. The standard ESPRIT algorithm for one-dimensional (1-D) arrays is reviewed in Section 63.2. There are three primary steps in any ESPRIT-type algorithm:

1. **Signal Subspace Estimation** computation of a basis for the estimated signal subspace,
2. **Solution of the Invariance Equation** solution of an (in general) overdetermined system of equations, the so-called invariance equation, derived from the basis matrix estimated in Step 1, and
3. **Spatial Frequency Estimation** computation of the eigenvalues of the solution of the invariance equation formed in Step 2.

Many antenna arrays used in practice have geometries that possess some form of symmetry. For example, a linear array of equi-spaced identical antennas is symmetric about the center of the linear aperture it occupies. In Section 63.3.1, an efficient implementation of ESPRIT is presented that exploits the symmetry present in so-called centro-symmetric arrays to formulate the three steps of ESPRIT in terms of real-valued computations, despite the fact that the input to the algorithm needs to be the complex analytic signal output from each antenna. This reduces the computational complexity significantly. A reduced dimension beamspace version of ESPRIT is developed in Section 63.3.2. Advantages to working in beamspace include reduced computational complexity [3], decreased sensitivity to array imperfections [1], and lower SNR resolution thresholds [11].

With a 1-D array, one can only estimate the angle of each incident plane wave relative to the array axis. For source localization purposes, this only places the source on a cone whose axis of symmetry is the array axis. The use of a 2-D or planar array enables one to passively estimate the 2-D arrival angles of each emitting source. The remainder of the chapter presents ESPRIT-based techniques for use in conjunction with circular and rectangular arrays that provide estimates of the azimuth and elevation angle of each incident signal. As in the 1-D case, the symmetries present in these array geometries are exploited to formulate the three primary steps of ESPRIT in terms of real-valued computations.

63.1.1 Notation

Throughout this chapter, column vectors and matrices are denoted by lower case and upper case boldfaced letters, respectively. For any positive integer p, $\boldsymbol{I}_p$ is the $p \times p$ identity matrix and $\boldsymbol{\Pi}_p$ the $p \times p$ exchange matrix with ones on its antidiagonal and zeros elsewhere,

$$\boldsymbol{\Pi}_p = \begin{bmatrix} & & & 1 \\ & & 1 & \\ & \cdot & & \\ 1 & & & \end{bmatrix} \in \mathbb{R}^{p \times p}. \tag{63.1}$$

Pre-multiplication of a matrix by $\boldsymbol{\Pi}_p$ will reverse the order of its rows, while post-multiplication of a matrix by $\boldsymbol{\Pi}_p$ reverses the order of its columns. Furthermore, the superscripts $(\cdot)^H$ and $(\cdot)^T$ denote complex conjugate transposition and transposition without complex conjugation, respectively. Complex conjugation by itself is denoted by an overbar $\overline{(\cdot)}$, such that $\boldsymbol{X}^H = \overline{\boldsymbol{X}}^T$. A diagonal matrix $\boldsymbol{\Phi}$ with the diagonal elements $\phi_1, \phi_2, \ldots, \phi_d$ may be written as

$$\boldsymbol{\Phi} = \mathrm{diag}\,\{\phi_i\}_{i=1}^d = \begin{bmatrix} \phi_1 & & & \\ & \phi_2 & & \\ & & \cdot & \\ & & & \phi_d \end{bmatrix} \in \mathbb{C}^{d \times d}.$$

Moreover, matrices $\boldsymbol{Q} \in \mathbb{C}^{p \times q}$ satisfying

$$\boldsymbol{\Pi}_p \overline{\boldsymbol{Q}} = \boldsymbol{Q} \tag{63.2}$$

will be called left $\boldsymbol{\Pi}$-real [10]. Often left $\boldsymbol{\Pi}$-real matrices are also called conjugate centro-symmetric [24].

63.2 The Standard ESPRIT Algorithm

The algorithm ESPRIT [18] must be used in conjunction with an M-element sensor array composed of m pairs of pairwise identical, but displaced, sensors (doublets) as depicted in Fig. 63.1. If the subarrays do not overlap, i.e., if they do not share any elements, $M = 2m$, but in general $M \leq 2m$ since overlapping subarrays are allowed, cf. Fig. 63.2. Let Δ denote the distance between the two subarrays. Incident on both subarrays are d narrowband noncoherent[1] planar wavefronts with distinct directions

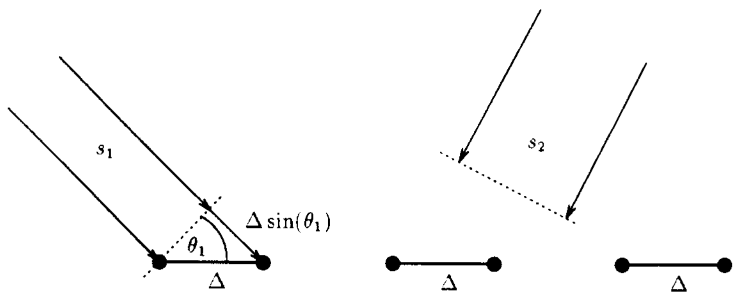

FIGURE 63.1: Planar array composed of $m = 3$ pairwise identical, but displaced, sensors (doublets).

of arrival (DOAs) θ_i, $1 \leq i \leq d$, relative to the displacement between the two subarrays.[2] Their complex pre-envelope at an arbitrary reference point may be expressed as $s_i(t) = \alpha_i(t) e^{\mathrm{j}(2\pi f_c t + \beta_i(t))}$, where f_c denotes the common carrier frequency of the d wavefronts. Without loss of generality, we assume that the reference point is the array centroid. The signals are called *narrowband* if their amplitudes $\alpha_i(t)$ and phases $\beta_i(t)$ vary slowly with respect to the propagation time across the array τ, i.e., if

$$\alpha_i(t-\tau) \approx \alpha_i(t) \quad \text{and} \quad \beta_i(t-\tau) \approx \beta_i(t). \tag{63.3}$$

In other words, the narrowband assumption allows the time-delay of the signals across the array τ to be modeled as a simple phase shift of the carrier frequency, such that

$$s_i(t-\tau) \approx \alpha_i(t) e^{\mathrm{j}(2\pi f_c (t-\tau) + \beta_i(t))} = e^{-\mathrm{j}2\pi f_c \tau} s_i(t).$$

Figure 63.1 shows that the propagation delay of a plane wave signal between the two identical sensors of a doublet equals $\tau_i = \frac{\Delta \sin\theta_i}{c}$, where c denotes the signal propagation velocity. Due to the narrowband assumption (63.3), this propagation delay τ_i corresponds to the multiplication of the complex envelope signal by the complex exponential $e^{\mathrm{j}\mu_i}$, referred to as the phase factor, such that

$$s_i(t-\tau_i) = e^{-\mathrm{j}\frac{2\pi f_c}{c}\Delta \sin\theta_i} s_i(t) = e^{\mathrm{j}\mu_i} s_i(t), \tag{63.4}$$

where the *spatial frequencies* μ_i are given by $\mu_i = -\frac{2\pi}{\lambda}\Delta \sin\theta_i$. Here, $\lambda = \frac{c}{f_c}$ denotes the common wavelength of the signals. We also assume that there is a one-to-one correspondence between the

[1] This restriction can be modified later as Unitary ESPRIT can estimate the directions of arrival of two coherent wavefronts due to an inherent forward-backward averaging effect. Two wavefronts are called *coherent* if their cross-correlation coefficient has magnitude one. The directions of arrival of *more than two* coherent wavefronts can be estimated by using spatial smoothing as a preprocessing step.

[2] $\theta_k = 0$ corresponds to the direction perpendicular to Δ.

spatial frequencies $-\pi < \mu_i < \pi$ and the range of possible DOAs. Thus, the maximum range is achieved for $\Delta \leq \lambda/2$. In this case, the DOAs are restricted to the interval $-90° < \theta_i < 90°$ to avoid ambiguities.

In the sequel, the d impinging signals $s_i(t)$, $1 \leq i \leq d$, are combined to a column vector $\boldsymbol{s}(t)$. Then the noise-corrupted measurements taken at the M sensors at time t obey the linear model

$$\boldsymbol{x}(t) = \begin{bmatrix} \boldsymbol{a}(\mu_1) & \boldsymbol{a}(\mu_2) & \cdots & \boldsymbol{a}(\mu_d) \end{bmatrix} \begin{bmatrix} s_1(t) \\ s_2(t) \\ \vdots \\ s_d(t) \end{bmatrix} + \boldsymbol{n}(t) = \boldsymbol{A}\boldsymbol{s}(t) + \boldsymbol{n}(t) \in \mathbb{C}^M, \tag{63.5}$$

where the columns of the array steering matrix $\boldsymbol{A} \in \mathbb{C}^{M \times d}$, the array response or array steering vectors $\boldsymbol{a}(\mu_i)$, are functions of the unknown spatial frequencies μ_i, $1 \leq i \leq d$. For example, for a uniform linear array (ULA) of M identical omnidirectional antennas,

$$\boldsymbol{a}(\mu_i) = e^{-\mathrm{j}\left(\frac{M-1}{2}\right)\mu_i} \begin{bmatrix} 1 & e^{\mathrm{j}\mu_i} & e^{\mathrm{j}2\mu_i} & \cdots & e^{\mathrm{j}(M-1)\mu_i} \end{bmatrix}^T, \quad 1 \leq i \leq d.$$

Moreover, the additive noise vector $\boldsymbol{n}(t)$ is taken from a zero-mean, spatially uncorrelated random process with variance σ_N^2, which is also uncorrelated with the signals. Since every row of $\boldsymbol{A}$ corresponds to an element of the sensor array, a particular subarray configuration can be described by two selection matrices, each choosing m elements of $\boldsymbol{x}(t) \in \mathbb{C}^M$, where m, $d \leq m < M$, is the number of elements in each subarray. Figure 63.2, for example, displays the appropriate subarray choices for three centro-symmetric arrays of $M = 6$ identical sensors.

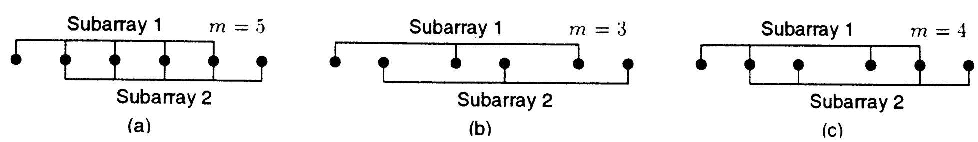

FIGURE 63.2: Three centro-symmetric line arrays of $M = 6$ identical sensors and the corresponding subarrays required for ESPRIT-type algorithms.

In case of a ULA with maximum overlap, cf. Figure 63.2 (a), $\boldsymbol{J}_1$ picks the first $m = M - 1$ rows of $\boldsymbol{A}$, while $\boldsymbol{J}_2$ selects the last $m = M - 1$ rows of the array steering matrix. In this case, the corresponding selection matrices are given by

$$\boldsymbol{J}_1 = \begin{bmatrix} 1 & 0 & 0 & \cdots & 0 & 0 \\ 0 & 1 & 0 & \cdots & 0 & 0 \\ \vdots & \vdots & \vdots & \ddots & \vdots & \vdots \\ 0 & 0 & 0 & \cdots & 1 & 0 \end{bmatrix} \in \mathbb{R}^{m \times M} \quad \text{and} \quad \boldsymbol{J}_2 = \begin{bmatrix} 0 & 1 & 0 & \cdots & 0 & 0 \\ 0 & 0 & 1 & \cdots & 0 & 0 \\ \vdots & \vdots & \vdots & \ddots & \vdots & \vdots \\ 0 & 0 & 0 & \cdots & 0 & 1 \end{bmatrix} \in \mathbb{R}^{m \times M}.$$

Notice that $\boldsymbol{J}_1$ and $\boldsymbol{J}_2$ are centro-symmetric with respect to one another, i.e., they obey $\boldsymbol{J}_2 = \boldsymbol{\Pi}_m \boldsymbol{J}_1 \boldsymbol{\Pi}_M$. This property holds for all centro-symmetric arrays and plays a key role in the derivation of Unitary ESPRIT [7]. Since we have two identical, but physically displaced subarrays, Eq. (63.4) indicates that an array steering vector of the *second* subarray $\boldsymbol{J}_2\boldsymbol{a}(\mu_i)$ is just a scaled version of the corresponding array steering vector of the *first* subarray $\boldsymbol{J}_1\boldsymbol{a}(\mu_i)$, namely

$$\boldsymbol{J}_1\boldsymbol{a}(\mu_i)e^{\mathrm{j}\mu_i} = \boldsymbol{J}_2\boldsymbol{a}(\mu_i), \quad 1 \leq i \leq d. \tag{63.6}$$

This *shift invariance property* of all d array steering vectors $\boldsymbol{a}(\mu_i)$ may be expressed in compact form as

$$\boldsymbol{J}_1\boldsymbol{A}\boldsymbol{\Phi} = \boldsymbol{J}_2\boldsymbol{A}, \quad \text{where} \quad \boldsymbol{\Phi} = \operatorname{diag}\left\{e^{\mathrm{j}\mu_i}\right\}_{i=1}^{d} \tag{63.7}$$

is the unitary diagonal $d \times d$ matrix of the phase factors. All ESPRIT-type algorithms are based on this invariance property of the array steering matrix $\boldsymbol{A}$, where $\boldsymbol{A}$ is assumed to have full column rank d.

Let $\boldsymbol{X}$ denote an $M \times N$ complex data matrix composed of N snapshots $\boldsymbol{x}(t_n)$, $1 \leq n \leq N$,

$$\begin{aligned} \boldsymbol{X} &= \begin{bmatrix} \boldsymbol{x}(t_1) & \boldsymbol{x}(t_2) & \cdots & \boldsymbol{x}(t_N) \end{bmatrix} \\ &= \boldsymbol{A}\begin{bmatrix} \boldsymbol{s}(t_1) & \boldsymbol{s}(t_2) & \cdots & \boldsymbol{s}(t_N) \end{bmatrix} + \begin{bmatrix} \boldsymbol{n}(t_1) & \boldsymbol{n}(t_2) & \cdots & \boldsymbol{n}(t_N) \end{bmatrix} \\ &= \boldsymbol{A} \cdot \boldsymbol{S} + \boldsymbol{N} \in \mathbb{C}^{M \times N}. \end{aligned} \tag{63.8}$$

The starting point is a singular value decomposition (SVD) of the noise-corrupted data matrix $\boldsymbol{X}$ (direct data approach). Assume that $\boldsymbol{U}_s \in \mathbb{C}^{M \times d}$ contains the d left singular vectors corresponding to the d largest singular values of $\boldsymbol{X}$. Alternatively, $\boldsymbol{U}_s$ can be obtained via an eigendecomposition of the (scaled) sample covariance matrix $\boldsymbol{X}\boldsymbol{X}^H$ (covariance approach). Then, $\boldsymbol{U}_s \in \mathbb{C}^{M \times d}$ contains the d eigenvectors corresponding to the d largest eigenvalues of $\boldsymbol{X}\boldsymbol{X}^H$.

Asymptotically, i.e., as the number of snapshots N becomes infinitely large, the range space of $\boldsymbol{U}_s$ is the d-dimensional range space of the array steering matrix $\boldsymbol{A}$ referred to as the *signal subspace*. Therefore, there exists a nonsingular $d \times d$ matrix $\boldsymbol{T}$ such that $\boldsymbol{A} \approx \boldsymbol{U}_s\boldsymbol{T}$. Let us express the shift-invariance property (63.7) in terms of the matrix $\boldsymbol{U}_s$ that spans the estimated signal subspace,

$$\boldsymbol{J}_1\boldsymbol{U}_s\boldsymbol{T}\boldsymbol{\Phi} \approx \boldsymbol{J}_2\boldsymbol{U}_s\boldsymbol{T} \iff \boldsymbol{J}_1\boldsymbol{U}_s\boldsymbol{\Psi} \approx \boldsymbol{J}_2\boldsymbol{U}_s, \quad \text{where} \quad \boldsymbol{\Psi} = \boldsymbol{T}\boldsymbol{\Phi}\boldsymbol{T}^{-1}$$

is a nonsingular $d \times d$ matrix. Since $\boldsymbol{\Phi}$ in Eq. (63.7) is diagonal, $\boldsymbol{T}\boldsymbol{\Phi}\boldsymbol{T}^{-1}$ is in the form of an eigenvalue decomposition. This implies that $e^{\mathrm{j}\mu_i}$, $1 \leq i \leq d$, are the eigenvalues of $\boldsymbol{\Psi}$. These observations form the basis for the subsequent steps of the algorithm. By applying the two selection matrices to the signal subspace matrix, the following (in general) overdetermined set of equations is formed,

$$\boldsymbol{J}_1\boldsymbol{U}_s\boldsymbol{\Psi} \approx \boldsymbol{J}_2\boldsymbol{U}_s \in \mathbb{C}^{m \times d}. \tag{63.9}$$

This set of equations, the so-called invariance equation, is usually solved in the least squares (LS) or total least squares (TLS) sense. Notice, however, that Eq. (63.9) is highly structured if overlapping subarray configurations are used. Structured least squares (SLS) is a new algorithm to solve the invariance equation by preserving its structure [8]. Formally, SLS was derived as a linearized iterative solution of a nonlinear optimization problem. If SLS is initialized with the LS solution of the invariance equation, only one "iteration", i.e., the solution of one linear system of equations, is required to achieve a significant improvement of the estimation accuracy [8].

Then an eigendecomposition of the resulting solution $\boldsymbol{\Psi} \in \mathbb{C}^{d \times d}$ may be expressed as

$$\boldsymbol{\Psi} = \boldsymbol{T}\boldsymbol{\Phi}\boldsymbol{T}^{-1} \quad \text{with} \quad \boldsymbol{\Phi} = \operatorname{diag}\left\{\phi_i\right\}_{i=1}^{d}. \tag{63.10}$$

The eigenvalues ϕ_i, i.e., the diagonal elements of $\boldsymbol{\Phi}$, represent estimates of the phase factors $e^{\mathrm{j}\mu_i}$. Notice that the ϕ_i are not guaranteed to be on the unit circle. Notwithstanding, estimates of the spatial frequencies μ_i and the corresponding DOAs θ_i are obtained via the relationships,

$$\mu_i = \arg(\phi_i) \quad \text{and} \quad \theta_i = -\frac{\lambda}{2\pi\Delta}\arcsin(\mu_i), \quad 1 \leq i \leq d. \tag{63.11}$$

To end this section, a brief summary of the standard ESPRIT algorithm is given in Table 63.1.

TABLE 63.1 Summary of the Standard ESPRIT Algorithm

1. *Signal Subspace Estimation:* Compute $\boldsymbol{U}_s \in \mathbb{C}^{M \times d}$ as the d dominant left singular vectors of $\boldsymbol{X} \in \mathbb{C}^{M \times N}$.

2. *Solution of the Invariance Equation:* Solve

$$\underbrace{\boldsymbol{J}_1 \boldsymbol{U}_s}_{\mathbb{C}^{m \times d}} \boldsymbol{\Psi} \approx \underbrace{\boldsymbol{J}_2 \boldsymbol{U}_s}_{\mathbb{C}^{m \times d}}$$

by means of LS, TLS, or SLS.

3. *Spatial Frequency Estimation:* Calculate the eigenvalues of the resulting complex-valued solution

$$\boldsymbol{\Psi} = \boldsymbol{T}\,\boldsymbol{\Phi}\,\boldsymbol{T}^{-1} \in \mathbb{C}^{d \times d} \quad \text{with} \quad \boldsymbol{\Phi} = \operatorname{diag}\{\phi_i\}_{i=1}^{d}$$

- $\mu_i = \arg(\phi_i)\,, \qquad 1 \le i \le d$

63.3 1-D Unitary ESPRIT

In contrast to the standard ESPRIT algorithm, Unitary ESPRIT is efficiently formulated in terms of real-valued computations throughout [7]. It is applicable to centro-symmetric array configurations that possess the discussed invariance structure, cf. Figs. 63.1 and 63.2. A sensor array is called *centro-symmetric* [23] if its element locations are symmetric with respect to the centroid. If the sensor elements have identical radiation characteristics, the array steering matrix of a centro-symmetric array satisfies

$$\boldsymbol{\Pi}_M \overline{\boldsymbol{A}} = \boldsymbol{A}, \tag{63.12}$$

since the array centroid is chosen as the phase reference.

63.3.1 1-D Unitary ESPRIT in Element Space

Before presenting an efficient element space implementation of Unitary ESPRIT, let us define the sparse unitary matrices

$$\boldsymbol{Q}_{2n} = \frac{1}{\sqrt{2}} \begin{bmatrix} \boldsymbol{I}_n & \mathrm{j}\boldsymbol{I}_n \\ \boldsymbol{\Pi}_n & -\mathrm{j}\boldsymbol{\Pi}_n \end{bmatrix} \quad \text{and} \quad \boldsymbol{Q}_{2n+1} = \frac{1}{\sqrt{2}} \begin{bmatrix} \boldsymbol{I}_n & \boldsymbol{0} & \mathrm{j}\boldsymbol{I}_n \\ \boldsymbol{0}^T & \sqrt{2} & \boldsymbol{0}^T \\ \boldsymbol{\Pi}_n & \boldsymbol{0} & -\mathrm{j}\boldsymbol{\Pi}_n \end{bmatrix}. \tag{63.13}$$

They are left $\boldsymbol{\Pi}$-real matrices of even and odd order, respectively.

Since Unitary ESPRIT involves forward-backward averaging, it can efficiently be formulated in terms of real-valued computations throughout, due to a one-to-one mapping between centro-Hermitian and real matrices [10]. The forward-backward averaged sample covariance matrix is centro-Hermitian and can, therefore, be transformed into a real-valued matrix of the same size, cf. [12], [15], and [7]. A real-valued square-root factor of this transformed sample covariance matrix is given by

$$\mathcal{T}(\boldsymbol{X}) = \boldsymbol{Q}_M^H \begin{bmatrix} \boldsymbol{X} & \boldsymbol{\Pi}_M \overline{\boldsymbol{X}} \boldsymbol{\Pi}_N \end{bmatrix} \boldsymbol{Q}_{2N} \in \mathbb{R}^{M \times 2N}, \tag{63.14}$$

where $\boldsymbol{Q}_M$ and $\boldsymbol{Q}_{2N}$ were defined in Eq. (63.13).[3] If M is even, an efficient computation of $\mathcal{T}(\boldsymbol{X})$ from the complex-valued data matrix $\boldsymbol{X}$ only requires $M \times 2N$ real additions and no multiplication [7]. Instead of computing a complex-valued SVD as in the standard ESPRIT case, the signal subspace estimate is obtained via a real-valued SVD of $\mathcal{T}(\boldsymbol{X})$ (direct data approach). Let $\boldsymbol{E}_s \in \mathbb{R}^{M \times d}$ contain the d left singular vectors corresponding to the d largest singular values of $\mathcal{T}(\boldsymbol{X})$.[4] Then the columns

[3] The results of this chapter also hold if $\boldsymbol{Q}_M$ and $\boldsymbol{Q}_{2N}$ denote arbitrary left $\boldsymbol{\Pi}$-real matrices that are also unitary.

[4] Alternatively, $\boldsymbol{E}_s$ can be obtained through a real-valued eigendecomposition of $\mathcal{T}(\boldsymbol{X})\mathcal{T}(\boldsymbol{X})^H$ (covariance approach).

of

$$\boldsymbol{U}_s = \boldsymbol{Q}_M \boldsymbol{E}_s \tag{63.15}$$

span the estimated signal subspace, and spatial frequency estimates could be obtained from the eigenvalues of the complex-valued matrix $\boldsymbol{\Psi}$ that solves Eq. (63.9). These complex-valued computations, however, are not required because the transformed array steering matrix

$$\boldsymbol{D} = \boldsymbol{Q}_M^H \boldsymbol{A} = \begin{bmatrix} \boldsymbol{d}(\mu_1) & \boldsymbol{d}(\mu_2) & \cdots & \boldsymbol{d}(\mu_d) \end{bmatrix} \in \mathbb{R}^{M \times d} \tag{63.16}$$

satisfies the following shift invariance property

$$\boldsymbol{K}_1 \boldsymbol{D}\, \boldsymbol{\Omega} = \boldsymbol{K}_2 \boldsymbol{D}, \quad \text{where} \quad \boldsymbol{\Omega} = \operatorname{diag}\left\{ \tan\left(\frac{\mu_i}{2}\right)\right\}_{i=1}^{d} \tag{63.17}$$

and the transformed selection matrices $\boldsymbol{K}_1$ and $\boldsymbol{K}_2$ are given by

$$\boldsymbol{K}_1 = 2 \cdot \operatorname{Re}\{\boldsymbol{Q}_m^H \boldsymbol{J}_2\, \boldsymbol{Q}_M\} \quad \text{and} \quad \boldsymbol{K}_2 = 2 \cdot \operatorname{Im}\{\boldsymbol{Q}_m^H \boldsymbol{J}_2\, \boldsymbol{Q}_M\}. \tag{63.18}$$

Here, $\operatorname{Re}\{\cdot\}$ and $\operatorname{Im}\{\cdot\}$ denote the real and the imaginary part, respectively. Notice that Eq. (63.17) is similar to Eq. (63.7) except for the fact that all matrices in Eq. (63.17) are real-valued.

Let us take a closer look at the transformed selection matrices defined in Eq. (63.18). If $\boldsymbol{J}_2$ is sparse, $\boldsymbol{K}_1$ and $\boldsymbol{K}_2$ are also sparse. This is illustrated by the following example. For the ULA with $M = 6$ sensors and maximum overlap sketched in Fig. 63.2 (a), $\boldsymbol{J}_2$ is given by

$$\boldsymbol{J}_2 = \begin{bmatrix} 0 & 1 & 0 & 0 & 0 & 0 \\ 0 & 0 & 1 & 0 & 0 & 0 \\ 0 & 0 & 0 & 1 & 0 & 0 \\ 0 & 0 & 0 & 0 & 1 & 0 \\ 0 & 0 & 0 & 0 & 0 & 1 \end{bmatrix} \in \mathbb{R}^{5 \times 6}.$$

According to Eq. (63.18), straightforward calculations yield the transformed selection matrices

$$\boldsymbol{K}_1 = \begin{bmatrix} 1 & 1 & 0 & 0 & 0 & 0 \\ 0 & 1 & 1 & 0 & 0 & 0 \\ 0 & 0 & \sqrt{2} & 0 & 0 & 0 \\ 0 & 0 & 0 & 1 & 1 & 0 \\ 0 & 0 & 0 & 0 & 1 & 1 \end{bmatrix} \quad \text{and} \quad \boldsymbol{K}_2 = \begin{bmatrix} 0 & 0 & 0 & -1 & 1 & 0 \\ 0 & 0 & 0 & 0 & -1 & 1 \\ 0 & 0 & 0 & 0 & 0 & -\sqrt{2} \\ 1 & -1 & 0 & 0 & 0 & 0 \\ 0 & 1 & -1 & 0 & 0 & 0 \end{bmatrix}.$$

In this case, applying $\boldsymbol{K}_1$ or $\boldsymbol{K}_2$ to $\boldsymbol{E}_s$ only requires $(m-1)d$ real additions and d real multiplications.

Asymptotically, the real-valued matrices $\boldsymbol{E}_s$ and $\boldsymbol{D}$ span the same d-dimensional subspace, i.e., there is a nonsingular matrix $\boldsymbol{T} \in \mathbb{R}^{d \times d}$ such that $\boldsymbol{D} \approx \boldsymbol{E}_s \boldsymbol{T}$. Substituting this into Eq. (63.17) yields the real-valued invariance equation

$$\boldsymbol{K}_1 \boldsymbol{E}_s\, \boldsymbol{\Upsilon} \approx \boldsymbol{K}_2 \boldsymbol{E}_s \in \mathbb{R}^{m \times d}, \quad \text{where} \quad \boldsymbol{\Upsilon} = \boldsymbol{T}\, \boldsymbol{\Omega}\, \boldsymbol{T}^{-1}. \tag{63.19}$$

Thus, the eigenvalues of the solution $\boldsymbol{\Upsilon} \in \mathbb{R}^{d \times d}$ to the matrix equation above are

$$\omega_i = \tan\left(\frac{\mu_i}{2}\right) = \frac{1}{\mathrm{j}} \frac{e^{\mathrm{j}\mu_i} - 1}{e^{\mathrm{j}\mu_i} + 1}, \qquad 1 \le i \le d. \tag{63.20}$$

This reveals a spatial frequency warping identical to the temporal frequency warping incurred in designing a digital filter from an analog filter via the bilinear transformation. Consider $\Delta = \frac{\lambda}{2}$ so that $\mu_i = -\frac{2\pi}{\lambda} \Delta \sin\theta_i = -\pi \sin\theta_i$. In this case, there is a one-to-one mapping between

$-1 < \sin\theta_i < 1$, corresponding to the range of possible values for the DOAs $-90° < \theta_i < 90°$, and $-\infty < \omega_i < \infty$.

Note that the fact that the eigenvalues of a real matrix have to either be real-valued or occur in complex conjugate pairs gives rise to an ad-hoc *reliability test*. That is, if the final step of the algorithm yields a complex conjugate pair of eigenvalues, then either the SNR is too low, not enough snapshots have been averaged, or two corresponding signal arrivals have not been resolved. In the latter case, taking the tangent inverse of the real part of the eigenvalues can sometimes provide a rough estimate of the direction of arrival of the two closely spaced signals. In general, though, if the algorithm yields one or more complex-conjugate pairs of eigenvalues in the final stage, the estimates should be viewed as unreliable.

The element space implementation of 1-D Unitary ESPRIT is summarized in Table 63.2.

TABLE 63.2 Summary of 1-D Unitary ESPRIT in Element Space

1. *Signal Subspace Estimation:* Compute $\boldsymbol{E}_s \in \mathbb{R}^{M\times d}$ as the d dominant left singular vectors of $\mathcal{T}(\boldsymbol{X}) \in \mathbb{R}^{M\times 2N}$.

2. *Solution of the Invariance Equation:* Then solve

$$\underbrace{\boldsymbol{K}_1\boldsymbol{E}_s}_{\mathbb{R}^{m\times d}}\,\boldsymbol{\Upsilon} \approx \underbrace{\boldsymbol{K}_2\boldsymbol{E}_s}_{\mathbb{R}^{m\times d}}$$

by means of LS, TLS, or SLS.

3. *Spatial Frequency Estimation:* Calculate the eigenvalues of the resulting real-valued solution

$$\boldsymbol{\Upsilon} = \boldsymbol{T}\,\boldsymbol{\Omega}\,\boldsymbol{T}^{-1} \in \mathbb{R}^{d\times d} \quad \text{with} \quad \boldsymbol{\Omega} = \operatorname{diag}\left\{\omega_i\right\}_{i=1}^{d}$$

- $\mu_i = 2\arctan\left(\omega_i\right), \qquad 1 \le i \le d$

63.3.2 1-D Unitary ESPRIT in DFT Beamspace

Reduced dimension processing in beamspace, yielding reduced computational complexity, is an option when one has *a priori* information on the general angular locations of the incident signals, as in a radar application, for example. In the case of a uniform linear array (ULA), transformation from element space to DFT beamspace may be effected by pre-multiplying the data by those rows of the DFT matrix that form beams encompassing the sector of interest. (Each row of the DFT matrix forms a beam pointed to a different angle.) If there is no *a priori* information, one may examine the DFT spectrum and apply Unitary ESPRIT in DFT beamspace to a small set of DFT values around each spectral peak above a particular threshold. In a more general setting, Unitary ESPRIT in DFT beamspace can simply be applied via parallel processing to each of a number of sets of successive DFT values corresponding to overlapping sectors.

Note, though, that in the development to follow, we will initially employ all M DFT beams for the sake of notational simplicity. Without loss of generality, we consider an omnidirectional ULA. Let $\boldsymbol{W}_M^H \in \mathbb{C}^{M\times M}$ be the scaled M-point DFT matrix with its M rows given by

$$\boldsymbol{w}_k^H = e^{\mathrm{j}\left(\frac{M-1}{2}\right)k\frac{2\pi}{M}} \begin{bmatrix} 1 & e^{-\mathrm{j}k\frac{2\pi}{M}} & e^{-\mathrm{j}2k\frac{2\pi}{M}} & \cdots & e^{-\mathrm{j}(M-1)k\frac{2\pi}{M}} \end{bmatrix}, \quad 0 \le k \le (M-1). \quad (63.21)$$

Notice that $\boldsymbol{W}_M$ is left $\boldsymbol{\Pi}$-real or column conjugate symmetric, i.e., $\boldsymbol{\Pi}_M\overline{\boldsymbol{W}}_M = \boldsymbol{W}_M$. Thus, as pointed out for $\boldsymbol{D}$ in Eq. (63.16), the transformed steering matrix of the ULA

$$\boldsymbol{B} = \boldsymbol{W}_M^H\boldsymbol{A} = \begin{bmatrix} \boldsymbol{b}(\mu_1) & \boldsymbol{b}(\mu_2) & \cdots & \boldsymbol{b}(\mu_d) \end{bmatrix} \in \mathbb{R}^{M\times d} \quad (63.22)$$

is real-valued. It has been shown in [24] that $\boldsymbol{B}$ satisfies a shift invariance property which is similar to Eq. (63.17), namely

$$\boldsymbol{\Gamma}_1 \boldsymbol{B}\, \boldsymbol{\Omega} = \boldsymbol{\Gamma}_2 \boldsymbol{B}, \quad \text{where} \quad \boldsymbol{\Omega} = \operatorname{diag}\left\{\tan\left(\frac{\mu_i}{2}\right)\right\}_{i=1}^{d}. \tag{63.23}$$

Here, the selection matrices $\boldsymbol{\Gamma}_1$ and $\boldsymbol{\Gamma}_2$ of size $M \times M$ are defined as

$$\boldsymbol{\Gamma}_1 = \begin{bmatrix} 1 & \cos\left(\frac{\pi}{M}\right) & 0 & 0 & \cdots & 0 & 0 \\ 0 & \cos\left(\frac{\pi}{M}\right) & \cos\left(\frac{2\pi}{M}\right) & 0 & \cdots & 0 & 0 \\ 0 & 0 & \cos\left(\frac{2\pi}{M}\right) & \cos\left(\frac{3\pi}{M}\right) & \cdots & 0 & 0 \\ \vdots & \vdots & \vdots & \vdots & \ddots & \vdots & \vdots \\ 0 & 0 & 0 & 0 & \cdots & \cos\left((M-2)\frac{\pi}{M}\right) & \cos\left((M-1)\frac{\pi}{M}\right) \\ (-1)^M & 0 & 0 & 0 & \cdots & 0 & \cos\left((M-1)\frac{\pi}{M}\right) \end{bmatrix} \tag{63.24}$$

$$\boldsymbol{\Gamma}_2 = \begin{bmatrix} 0 & \sin\left(\frac{\pi}{M}\right) & 0 & 0 & \cdots & 0 & 0 \\ 0 & \sin\left(\frac{\pi}{M}\right) & \sin\left(\frac{2\pi}{M}\right) & 0 & \cdots & 0 & 0 \\ 0 & 0 & \sin\left(\frac{2\pi}{M}\right) & \sin\left(\frac{3\pi}{M}\right) & \cdots & 0 & 0 \\ \vdots & \vdots & \vdots & \vdots & \ddots & \vdots & \vdots \\ 0 & 0 & 0 & 0 & \cdots & \sin\left((M-2)\frac{\pi}{M}\right) & \sin\left((M-1)\frac{\pi}{M}\right) \\ 0 & 0 & 0 & 0 & \cdots & 0 & \sin\left((M-1)\frac{\pi}{M}\right) \end{bmatrix}. \tag{63.25}$$

As an alternative to Eq. (63.14), another real-valued square-root factor of the transformed sample covariance matrix is given by

$$\begin{bmatrix} \operatorname{Re}\{\boldsymbol{Y}\} & \operatorname{Im}\{\boldsymbol{Y}\} \end{bmatrix} \in \mathbb{R}^{M \times 2N}, \quad \text{where} \quad \boldsymbol{Y} = \boldsymbol{W}_M^H \boldsymbol{X} \in \mathbb{C}^{M \times N}. \tag{63.26}$$

The matrix $\boldsymbol{Y}$ can efficiently be computed via an FFT, which exploits the Vandermonde form of the rows of the DFT matrix, followed by an appropriate scaling, cf. Eq. (63.21). Let the columns of $\boldsymbol{E}_s \in \mathbb{R}^{M \times d}$ contain the d left singular vectors corresponding to the d largest singular values of Eq. (63.26). Asymptotically, the real-valued matrices $\boldsymbol{E}_s$ and $\boldsymbol{B}$ span the same d-dimensional subspace, i.e., there is a nonsingular matrix $\boldsymbol{T} \in \mathbb{R}^{d \times d}$, such that $\boldsymbol{B} \approx \boldsymbol{E}_s \boldsymbol{T}$. Substituting this into Eq. (63.23), yields the real-valued invariance equation

$$\boldsymbol{\Gamma}_1 \boldsymbol{E}_s\, \boldsymbol{\Upsilon} \approx \boldsymbol{\Gamma}_2 \boldsymbol{E}_s \in \mathbb{R}^{M \times d}, \quad \text{where} \quad \boldsymbol{\Upsilon} = \boldsymbol{T}\, \boldsymbol{\Omega}\, \boldsymbol{T}^{-1}. \tag{63.27}$$

Thus, the eigenvalues of the solution $\boldsymbol{\Upsilon} \in \mathbb{R}^{d \times d}$ to the matrix equation above are also given by Eq. (63.20).

It is a crucial observation that one row of the matrix equation (63.23) relates *two successive components* of the transformed array steering vectors $\boldsymbol{b}(\mu_i)$, cf. (63.24) and (63.25). This insight enables us to apply only $B \ll M$ successive rows of $\boldsymbol{W}_M^H$ (instead of all M rows) to the data matrix $\boldsymbol{X}$ in Eq. (63.26). To stress the reduced number of rows, we call the resulting beamforming matrix $\boldsymbol{W}_B^H \in \mathbb{C}^{B \times M}$. The number of its rows, B, depends on the width of the sector of interest and may be substantially less than the number of sensors M. Thereby, the SVD of Eq. (63.26) and, therefore, also $\boldsymbol{E}_s \in \mathbb{R}^{B \times d}$ and the invariance equation (63.27) will have a reduced dimensionality. Employing the appropriate subblocks of $\boldsymbol{\Gamma}_1$ and $\boldsymbol{\Gamma}_2$ as selection matrices, the algorithm is the same as the one described previously except for its reduced dimensionality. In the sequel, the resulting selection matrices of size $(B-1) \times B$ will be called $\boldsymbol{\Gamma}_1^{(B)}$ and $\boldsymbol{\Gamma}_2^{(B)}$. The whole algorithm that operates in a B-dimensional DFT beamspace is summarized in Table 63.3.

Consider, for example, a ULA of $M = 8$ sensors. The structure of the corresponding selection matrices $\boldsymbol{\Gamma}_1$ and $\boldsymbol{\Gamma}_2$ is sketched in Fig. 63.3. Here, the symbol $\times$ denotes entries of both selection matrices that might be nonzero, cf. (63.24) and (63.25). If one employed rows 4, 5, and 6 of $\boldsymbol{W}_8^H$ to form $B = 3$ beams in estimating the DOAs of two closely spaced signal arrivals, as in the low-angle

TABLE 63.3 Summary of 1-D Unitary ESPRIT in DFT Beamspace

0. *Transformation to Beamspace:* $\boldsymbol{Y} = \boldsymbol{W}_B^H \boldsymbol{X} \in \mathbb{C}^{B \times N}$

1. *Signal Subspace Estimation:* Compute $\boldsymbol{E}_s \in \mathbb{R}^{B \times d}$ as the d dominant left singular vectors of $\begin{bmatrix} \mathrm{Re}\{\boldsymbol{Y}\} & \mathrm{Im}\{\boldsymbol{Y}\} \end{bmatrix} \in \mathbb{R}^{B \times 2N}$.

2. *Solution of the Invariance Equation:* Solve

$$\underbrace{\boldsymbol{\Gamma}_1^{(B)} \boldsymbol{E}_s}_{\mathbb{R}^{(B-1)\times d}} \boldsymbol{\Upsilon} \approx \underbrace{\boldsymbol{\Gamma}_2^{(B)} \boldsymbol{E}_s}_{\mathbb{R}^{(B-1)\times d}}$$

by means of LS, TLS, or SLS.

3. *Spatial Frequency Estimation:* Calculate the eigenvalues of the resulting real-valued solution

$$\boldsymbol{\Upsilon} = \boldsymbol{T}\,\boldsymbol{\Omega}\,\boldsymbol{T}^{-1} \in \mathbb{R}^{d \times d} \quad \text{with} \quad \boldsymbol{\Omega} = \mathrm{diag}\,\{\omega_i\}_{i=1}^{d}$$

- $\mu_i = 2 \arctan(\omega_i), \qquad 1 \le i \le d$

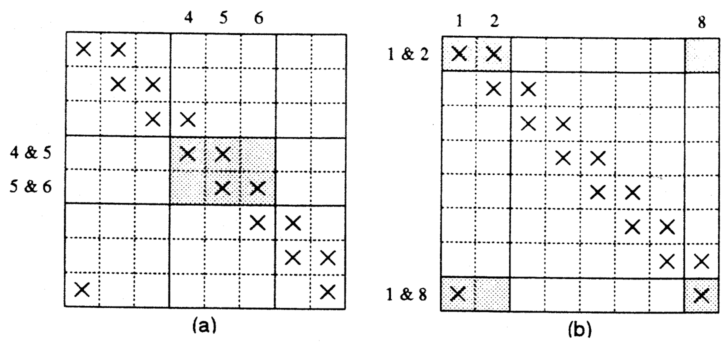

FIGURE 63.3: Structure of the selection matrices $\boldsymbol{\Gamma}_1$ and $\boldsymbol{\Gamma}_2$ for a ULA of $M = 8$ sensors. The symbol $\times$ denotes entries of both selection matrices that might be nonzero. The shaded areas illustrate how to choose the appropriate subblocks of the selection matrices for reduced dimension processing, i.e., how to form $\boldsymbol{\Gamma}_1^{(B)}$ and $\boldsymbol{\Gamma}_2^{(B)}$, if only $B = 3$ successive rows of $\boldsymbol{W}_8^H$ are applied to the data matrix $\boldsymbol{X}$. Here, the following two examples are used: (a) rows 4, 5, and 6. (b) rows 8, 1, and 2.

radar tracking scheme described by Zoltowski and Lee [26], the corresponding 2×3 subblock of the selection matrices $\boldsymbol{\Gamma}_1$ and $\boldsymbol{\Gamma}_2$ is shaded in Fig. 63.3 (a).[5] Notice that the first and the last (Mth) row of $\boldsymbol{W}_M^H$ steer beams that are also physically adjacent to one another (the wrap-around property of the DFT). If, for example, one employed rows 8, 1, and 2 of $\boldsymbol{W}_8^H$ to form $B = 3$ beams in estimating the DOAs of two closely spaced signal arrivals, the corresponding subblocks of the selection matrices $\boldsymbol{\Gamma}_1$ and $\boldsymbol{\Gamma}_2$ are shaded in Fig. 63.3 (b).[6]

[5] Here, the first row of $\boldsymbol{\Gamma}_1^{(3)}$ and $\boldsymbol{\Gamma}_2^{(3)}$ combines beams 4 and 5, while the second row of $\boldsymbol{\Gamma}_1^{(3)}$ and $\boldsymbol{\Gamma}_2^{(3)}$ combines beams 5 and 6.

[6] Here, the first row of $\boldsymbol{\Gamma}_1^{(3)}$ and $\boldsymbol{\Gamma}_2^{(3)}$ combines beams 1 and 2, while the second row of $\boldsymbol{\Gamma}_1^{(3)}$ and $\boldsymbol{\Gamma}_2^{(3)}$ combines beams 1 and 8.

63.4 UCA-ESPRIT for Circular Ring Arrays

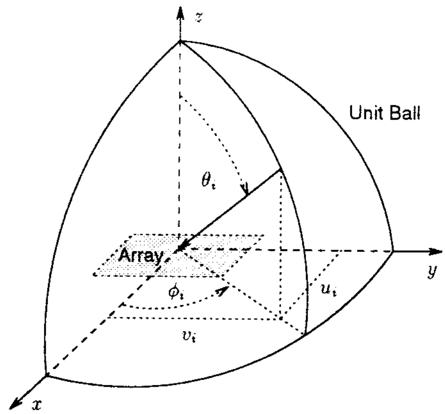

FIGURE 63.4: Definitions of azimuth ($-180° < \phi_i \leq 180°$) and elevation ($0° \leq \theta_i \leq 90°$). The direction cosines u_i and v_i are the rectangular coordinates of the projection of the corresponding point on the unit ball onto the equatorial plane.

UCA-ESPRIT [15, 16, 17] is a 2-D angle estimation algorithm developed for use with uniform circular arrays (UCAs). The algorithm provides automatically paired azimuth and elevation angle estimates of far-field signals incident on the UCA via a closed-form procedure. The rotational symmetry of the UCA makes it desirable for a variety of applications where one needs to discriminate in both azimuth and elevation, as opposed to just conical angle of arrival which is all the ULA can discriminate on. For example, UCAs are commonly employed as part of an anti-jam spatial filter for GPS receivers. Some experimental UCA based systems are described in [4]. The development of a closed-form 2-D angle estimation technique for a UCA provides further motivation for the use of a UCA in a given application.

Consider an M element UCA in which the array elements are uniformly distributed over the circumference of a circle of radius R. We will assume that the array is located in the x-y plane, with its center at the origin of the coordinate system. The elevation angles θ_i and azimuth angles ϕ_i of the d impinging sources are defined in Fig. 63.4, as are the direction cosines u_i and v_i, $1 \leq i \leq d$. UCA-ESPRIT is premised on phase mode excitation-based beamforming. The maximum phase mode (integer valued) excitable by a given UCA is

$$K \approx \frac{2\pi R}{\lambda},$$

where λ is the common (carrier) wavelength of the incident signals. Phase mode excitation-based beamforming requires $M > 2K$ array elements ($M = 2K + 3$ is usually adequate). UCA-ESPRIT can resolve a maximum of $d_{\max} = K - 1$ sources. As an example, if the array radius is $r = \lambda$, $K = 6$ (the largest integer smaller than 2π) and at least $M = 15$ array elements are needed. UCA-ESPRIT can resolve five sources in conjunction with this UCA.

UCA-ESPRIT operates in a $K' = 2K+1$ dimensional beamspace. It employs a $K' \times M$ beamforming matrix to transform from element space to beamspace. After this transformation, the algorithm has the same three basic steps of any ESPRIT-type algorithm: (1) the computation of a basis for the signal subspace, (2) the solution to an (in general) overdetermined system of equations derived from the matrix of vectors spanning the signal subspace, and (3) the computation of the eigenvalues of the solution to the system of equations formed in Step (2). As illustrated in Fig. 63.6, the ith eigenvalue obtained in the final step is ideally of the form $\xi_i = \sin\theta_i\, e^{\mathrm{j}\phi_i}$, where ϕ_i and θ_i are the azimuth and elevation angles of the ith source. Note that

$$\xi_i = \sin\theta_i\, e^{\mathrm{j}\phi_i} = u_i + \mathrm{j}v_i, \quad 1 \le i \le d,$$

where u_i and v_i are the direction cosines of the ith source relative to the x- and y-axis, respectively, as indicated in Fig. 63.4.

The formulation of UCA-ESPRIT is based on the special structure of the resulting K'-dimensional beamspace manifold. The following vector and matrix definitions are needed to summarize the algorithm in Table 63.4.

$$\boldsymbol{v}_k^H = \frac{1}{M}\begin{bmatrix} 1 & e^{\mathrm{j}k\frac{2\pi}{M}} & e^{\mathrm{j}2k\frac{2\pi}{M}} & \cdots & e^{\mathrm{j}(M-1)k\frac{2\pi}{M}} \end{bmatrix} \tag{63.28}$$

$$\boldsymbol{V} = \sqrt{M}\begin{bmatrix} \boldsymbol{v}_{-K} & \cdots & \boldsymbol{v}_{-1} & \boldsymbol{v}_0 & \boldsymbol{v}_1 & \cdots & \boldsymbol{v}_K \end{bmatrix} \in \mathbb{C}^{M\times K'}$$

$$\boldsymbol{C}_v = \mathrm{diag}\left\{\mathrm{j}^k\right\}_{k=-K}^{K} \in \mathbb{C}^{K'\times K'}$$

$$\boldsymbol{F}_r^H = \boldsymbol{Q}_{K'}^T \boldsymbol{C}_v \boldsymbol{V}^H \in \mathbb{C}^{K'\times M} \tag{63.29}$$

$$\boldsymbol{C}_o = \mathrm{diag}\left\{\mathrm{sign}(k)^{-k}\right\}_{k=-K}^{K} \in \mathbb{R}^{K'\times K'}$$

$$\boldsymbol{D} = \mathrm{diag}\left\{(-1)^{|k|}\right\}_{k=-(K-2)}^{K} \in \mathbb{R}^{(K'-2)\times(K'-2)}$$

$$\boldsymbol{\Gamma} = \frac{\lambda}{\pi r}\cdot \mathrm{diag}\left\{k\right\}_{k=-(K-1)}^{(K-1)} \in \mathbb{R}^{(K'-2)\times(K'-2)}$$

Note that the columns of the matrix $\boldsymbol{V}$ consist of the DFT weight vectors $\boldsymbol{v}_k$ defined in Eq. (63.28). The beamforming matrix $\boldsymbol{F}_r^H$ in Eq. (63.29) synthesizes a real-valued beamspace manifold and facilitates signal subspace estimation via a real-valued SVD or eigendecomposition. Recall that the sparse left $\boldsymbol{\Pi}$-real matrix $\boldsymbol{Q}_{K'} \in \mathbb{C}^{K'\times K'}$ has been defined in Eq. (63.13). The complete UCA-ESPRIT algorithm is summarized in Table 63.4.

63.4.1 Results of Computer Simulations

Simulations were conducted with a UCA of radius $R = \lambda$, with $K = 6$ and $M = 19$ (performance close to that reported below can be expected even if $M = 15$ elements are employed). The simulation employed two sources with arrival angles given by $(\theta_1, \phi_1) = (72.73°, 90°)$ and $(\theta_2, \phi_2) = (50.44°, 78°)$. The sources were highly correlated, with the correlation coefficient referred to the center of the array being $0.9e^{\mathrm{j}\frac{\pi}{4}}$. The signal-to-noise ratio (SNR) was 10 dB (per array element) for each source. The number of snapshots was $N = 64$, and arrival angle estimates were obtained for 200 independent trials. Figure 63.5 depicts the results of the simulation. Here, the UCA-ESPRIT eigenvalues ξ_i are denoted by the symbol $\times$.[7] The results from all 200 trials are superimposed in the figure. The eigenvalues are seen to be clustered around the expected locations (the dashed circles indicate the true elevation angles).

[7] The horizontal axis represents $\mathrm{Re}\{\xi_i\}$, and the vertical axis represents $\mathrm{Im}\{\xi_i\}$.

TABLE 63.4 Summary of UCA-ESPRIT

0. Transformation to Beamspace: $\boldsymbol{Y} = \boldsymbol{F}_r^H \boldsymbol{X} \in \mathbb{C}^{K' \times N}$
1. Signal Subspace Estimation: Compute $\boldsymbol{E}_s \in \mathbb{R}^{K' \times d}$ as the d dominant left singular vectors of $\left[\ \mathrm{Re}\{\boldsymbol{Y}\} \quad \mathrm{Im}\{\boldsymbol{Y}\}\ \right] \in \mathbb{R}^{K' \times 2N}$.
2. Solution of the Invariance Equation:
• Compute $\boldsymbol{E}_u = \boldsymbol{C}_o \overline{\boldsymbol{Q}}_{K'} \boldsymbol{E}_s$. Form the matrix $\boldsymbol{E}_{-1}$ that consists of all but the last two rows of $\boldsymbol{E}_u$. Similarly form the matrix $\boldsymbol{E}_0$ that consists of all but the first and last rows of $\boldsymbol{E}_u$.
• Compute $\underline{\boldsymbol{\Psi}} \in \mathbb{C}^{2d \times d}$, the least squares solution to the system $$\left[\ \boldsymbol{E}_{-1} \quad \boldsymbol{D}\boldsymbol{\Pi}_{(K'-2)}\overline{\boldsymbol{E}}_{-1}\ \right]\underline{\boldsymbol{\Psi}} = \boldsymbol{\Gamma}\boldsymbol{E}_0 \in \mathbb{C}^{(K'-2) \times d}.$$ Recall that the overbar denotes complex conjugation. Form $\boldsymbol{\Psi}$ by extracting the upper $d \times d$ block from $\underline{\boldsymbol{\Psi}}$. Note that $\boldsymbol{\Psi}$ can be computed efficiently by solving a *real-valued* system of $2d$ equations (see [17]).
3. Spatial Frequency Estimation: Compute the eigenvalues ξ_i, $1 \leq i \leq d$, of $\boldsymbol{\Psi} \in \mathbb{C}^{d \times d}$. The estimates of the elevation and azimuth angles of the ith source are $$\theta_i = \arcsin(\lvert\xi_i\rvert) \quad \text{and} \quad \phi_i = \arg(\xi_i),$$ respectively. If direction cosine estimates are desired, we have $$u_i = \mathrm{Re}\{\xi_i\} \quad \text{and} \quad v_i = \mathrm{Im}\{\xi_i\}.$$ Again, ξ_i can be efficiently computed via a *real-valued* EVD (see [17]).

63.5 FCA-ESPRIT for Filled Circular Arrays

The use of a circular ring array and the attendant use of UCA-ESPRIT is ideal for applications where the array aperture is not very large as on the top of a mobile communications unit. For much larger array apertures as in phased array surveillance radars, too much of the aperture is devoid of elements so that a lot of the signal energy impinging on the aperture is not intercepted. As an example, each of the four panels comprising either the SPY-1A or SPY-1B radars of the AEGIS series is composed of 4400 identical elements regularly spaced on a flat panel over a circular aperture [19]. The sampling lattice is hexagonal. Recent prototype arrays for satellite-based communications have also employed the filled circular array geometry [2].

This section presents an algorithm similar to UCA-ESPRIT that provides the same closed-form 2-D angle estimation capability for a *Filled Circular Array* (FCA). Similar to UCA-ESPRIT, the far field pattern arising from the sampled excitation is approximated by the far field pattern arising from the continuous excitation from which the sampled excitation is derived through sampling. (Note, Steinberg [20] shows that the array pattern for a ULA of N elements with interelement spacing d is nearly identical to the far field pattern for a continuous linear aperture of length $(N+1)d$, except near the fringes of the visible region.) That is, it is assumed that the interelement spacings have been chosen so that aliasing effects are negligible as in the generation of phase modes with a single ring array. It can be shown that this is the case for any sampling lattice as long as the inter-sensor spacings is roughly half a wavelength or less on the average and that the sources of interest are at least 20° in elevation above the plane of the array, i.e., we require that the elevation angle of the ith source satisfies $0 \leq \theta_i \leq 70°$. In practice, many phased arrays only provide reliable coverage for $0 \leq \theta_i \leq 60^o$ (plus or minus 60° away from boresite) due to a reduced aperture effect and the fact that the gain of each individual antenna has a significant roll-off at elevation angles near the horizon, i.e., the plane of the array. FCA-ESPRIT has been successfully applied to rectangular, hexagonal, polar raster, and random sampling lattices.

The key to the development of UCA-ESPRIT was phase-mode (DFT) excitation and exploitation of a recurrence relationship that Bessel functions satisfy. In the case of a filled circular array, the same

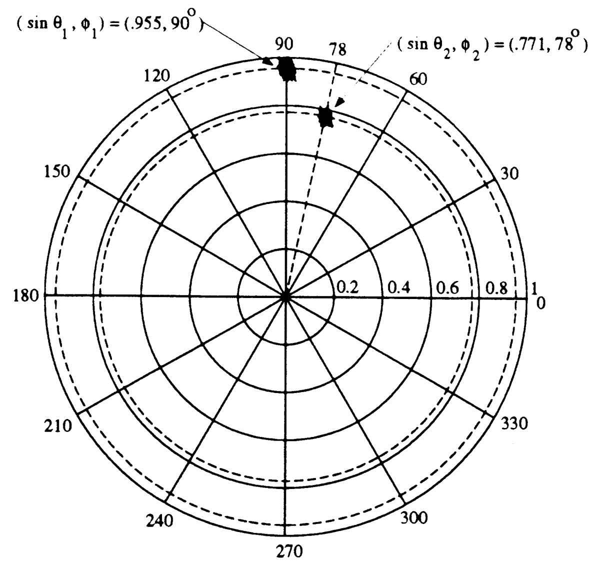

FIGURE 63.5: Plot of the UCA-ESPRIT eigenvalues $\xi_1 = \sin\theta_1 e^{j\phi_1}$ and $\xi_2 = \sin\theta_2 e^{j\phi_2}$ for 200 trials.

type of processing is facilitated by the use of a phase-mode dependent aperture taper derived from an integral relationship that Bessel functions satisfy.

Consider an M element FCA where the array elements are distributed over a circular aperture of radius R. We assume that the array is centered at the origin of the coordinate system and contained in the x-y plane. The ith element is located at a radial distance r_i from the origin and at an angle γ_i relative to the x-axis measured counter-clockwise in the x-y plane. In contrast to a UCA, $0 \leq r_i \leq R$, i.e., the elements lie within, rather than on, a circle of radius R. The beamforming weight vectors employed in FCA-ESPRIT are

$$\boldsymbol{w}_m = \frac{1}{M}\begin{bmatrix} A_1\left(\frac{r_1}{R}\right)^{|m|} e^{-jm\gamma_1} \\ \vdots \\ A_i\left(\frac{r_i}{R}\right)^{|m|} e^{-jm\gamma_i} \\ \vdots \\ A_M\left(\frac{r_M}{R}\right)^{|m|} e^{-jm\gamma_M} \end{bmatrix}, \tag{63.30}$$

where m ranges from $-K$ to K with $K \approx \frac{2\pi R}{\lambda}$. Here A_i is proportional to the area surrounding the ith array element. A_i is a constant (and can be omitted) for hexagonal and rectangular lattices and proportional to the radius ($A_i = r_i$) for a polar raster. The transformation from element space to beamspace is effected through pre-multiplication by the beamforming matrix

$$\boldsymbol{W} = \sqrt{M}\begin{bmatrix} \boldsymbol{w}_{-K} & \cdots & \boldsymbol{w}_{-1} & \boldsymbol{w}_0 & \boldsymbol{w}_1 & \cdots & \boldsymbol{w}_K \end{bmatrix} \in \mathbb{C}^{M\times K'}\ (K' = 2K+1). \tag{63.31}$$

The following matrix definitions are needed to summarize FCA-ESPRIT.

$$\begin{aligned} \boldsymbol{B} &= \boldsymbol{W}\boldsymbol{C} \in \mathbb{C}^{M\times K'} \\ \boldsymbol{C} &= \operatorname{diag}\left\{\operatorname{sign}(k)\cdot j^k\right\}_{k=-K}^{K} \in \mathbb{C}^{K'\times K'} \end{aligned} \tag{63.32}$$

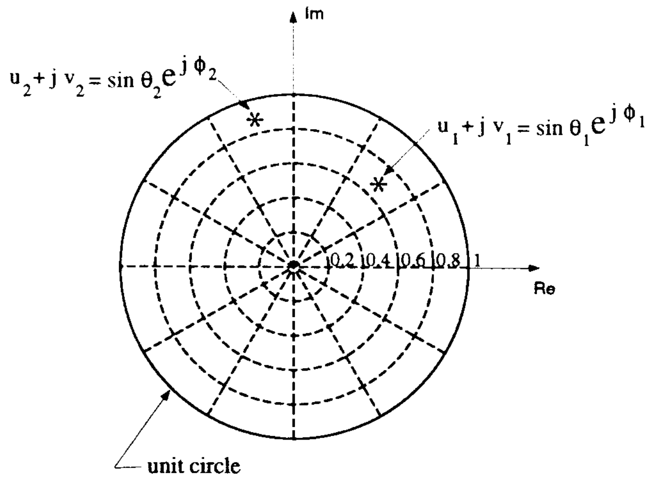

FIGURE 63.6: Illustrating the form of signal roots (eigenvalues) obtained with UCA-ESPRIT or FCA-ESPRIT.

$$
\begin{aligned}
\boldsymbol{B}_r &= \boldsymbol{B}\boldsymbol{F}\bar{\boldsymbol{Q}}_{K'} \in \mathbb{C}^{M\times K'} \\
\boldsymbol{F} &= \mathrm{diag}\left([(-1)^{-M-1}, \cdots, (-1)^{-2}, 1, 1, \cdots, 1]\right) \in \mathbb{R}^{K'\times K'} \\
\boldsymbol{\Gamma} &= \frac{\lambda}{\pi R}\mathrm{diag}([\overbrace{-M, \cdots, -3, -2}^{M-1}, 0, \overbrace{2, \cdots, M}^{M-1}]) \in \mathbb{R}^{(K'-2)\times(K'-2)} \\
\boldsymbol{C}_1 &= \mathrm{diag}([\overbrace{1, \cdots, 1}^{M-2}, -1, -1, \overbrace{1, \cdots, 1}^{M-1}]) \in \mathbb{R}^{(K'-2)\times(K'-2)}
\end{aligned}
$$

The whole algorithm is summarized in Table 63.5. The beamforming matrix $\boldsymbol{B}_r^H$ synthesizes a real-valued manifold that facilitates signal subspace estimation via a real-valued SVD or eigenvalue decomposition in the first step. As in UCA-ESPRIT, the eigenvalues of $\boldsymbol{\Psi}$ computed in the final step are asymptotically of the form $\sin(\theta_i)e^{j\phi_i}$, where θ_i and ϕ_i are the elevation and azimuth angles of the ith source, respectively.

63.5.1 Computer Simulation

As an example, a simulation involving a *random filled array* is presented. The element locations are depicted in Fig. 63.7. The outer radius is $R = 5\lambda$ and the average distance between elements is $\lambda/4$. Two plane waves of equal power were incident upon the array. The Signal to Noise Ratio (SNR) per antenna per signal was 0 dB. One signal arrived at 10° elevation and 40° azimuth, while the other arrived at 30° elevation and 60° azimuth. Figure 63.8 shows the results of 32 independent trials of FCA-ESPRIT overlaid; each execution of the algorithm (with a different realization of the noise) produced two eigenvalues. The eigenvalues are observed to be clustered around the expected locations (the dashed circles indicate the true elevation angles).

63.6 2-D Unitary ESPRIT

For uniform circular arrays and filled circular arrays, UCA-ESPRIT and FCA-ESPRIT provide closed-form, automatically paired 2-D angle estimates as long as the direction cosine pair of each signal arrival

TABLE 63.5 Summary of FCA-ESPRIT

0. *Transformation to Beamspace:* $\boldsymbol{Y} = \boldsymbol{B}_r^H \boldsymbol{X}$
1. *Signal Subspace Estimation:* Compute $\boldsymbol{E}_s \in \mathbb{R}^{K' \times d}$ as the d dominant left singular vector of $\begin{bmatrix} \mathrm{Re}\{\boldsymbol{Y}\} & \mathrm{Im}\{\boldsymbol{Y}\} \end{bmatrix} \in \mathbb{R}^{K' \times 2N}$.
2. *Solution of the Invariance Equation:*
• Compute $\boldsymbol{E}_u = \boldsymbol{F}\boldsymbol{Q}_{K'}\boldsymbol{E}_s$. Form the matrices $\boldsymbol{E}_{-1}$, $\boldsymbol{E}_0$, and $\boldsymbol{E}_1$ that consist of all but the last two, first and last, and first two rows, respectively.
• Compute $\underline{\boldsymbol{\Psi}} \in \mathbb{C}^{2d \times d}$, the least squares solution to the system $$\begin{bmatrix} \boldsymbol{E}_{-1} & \boldsymbol{C}_1\boldsymbol{E}_1 \end{bmatrix} \underline{\boldsymbol{\Psi}} = \boldsymbol{\Gamma}\boldsymbol{E}_0 \in \mathbb{C}^{(K'-2) \times d}.$$ Form $\boldsymbol{\Psi}$ by extracting the upper $d \times d$ block from $\underline{\boldsymbol{\Psi}}$.
3. *Spatial Frequency Estimation:* Compute the eigenvalues ξ_i, $1 \leq i \leq d$, of $\boldsymbol{\Psi} \in \mathbb{C}^{d \times d}$. The estimates of the elevation and azimuth angles of the ith source are $$\theta_i = \arcsin(\lvert\xi_i\rvert) \quad \text{and} \quad \phi_i = \arg(\xi_i),$$ respectively.

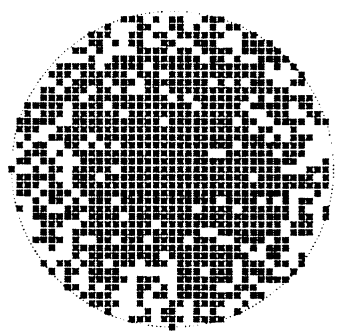

FIGURE 63.7: Random filled array.

is unique. In this section, we develop 2-D Unitary ESPRIT, a closed-form 2-D angle estimation algorithm that achieves automatic pairing in a similar fashion. It is applicable to 2-D centro-symmetric array configurations with a dual invariance structure such as uniform rectangular arrays (URAs). In the derivations of UCA-ESPRIT and FCA-ESPRIT it was necessary to approximate the sampled aperture pattern by the continuous aperture pattern. Such an approximation is not required in the development of 2-D Unitary ESPRIT.

Apart from the 2-D extension presented here, Unitary ESPRIT has also been extended to the R-dimensional case to solve the R-dimensional harmonic retrieval problem, where $R \geq 3$. R-D Unitary ESPRIT is a closed-form algorithm to estimate several undamped R-dimensional modes (or frequencies) along with their correct pairing. In [6], automatic pairing of the R-dimensional frequency estimates is achieved through a new simultaneous Schur decomposition of R real-valued, non-symmetric matrices that reveals their "average eigenstructure". Like its 1-D and 2-D counterparts, R-D Unitary ESPRIT inherently includes forward-backward averaging and is efficiently formulated in terms of real-valued computations throughout. In the array processing context, a three-dimensional extension of Unitary ESPRIT can be used to estimate the 2-D arrival angles and carrier frequencies of several impinging wavefronts simultaneously.

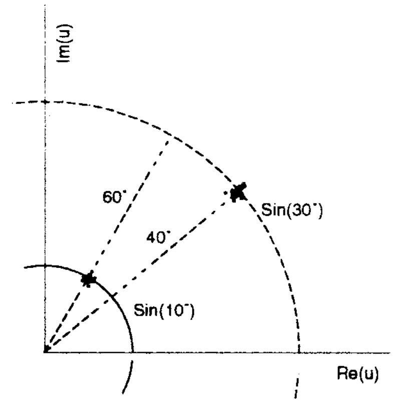

FIGURE 63.8: Plot of the FCA-ESPRIT eigenvalues from 32 independent trials.

63.6.1 2-D Array Geometry

Consider a 2-D centro-symmetric sensor array of M elements lying in the x-y plane (Fig. 63.4). Assume that the array also exhibits a *dual* invariance, i.e., two identical subarrays of m_x elements are displaced by Δ_x along the x-axis, and another pair of identical subarrays, consisting of m_y elements each, is displaced by Δ_y along the y-axis. Notice that the four subarrays can overlap and m_x is not required to equal m_y. Such array configurations include uniform rectangular arrays (URAs), uniform rectangular frame arrays (URFAs), i.e., URAs without some of their center elements, and cross arrays consisting of two orthogonal linear arrays with a common phase center as shown in Fig. 63.9.[8]

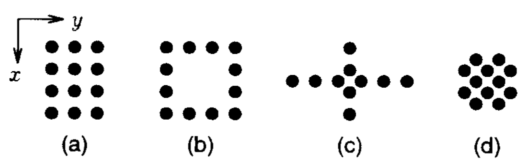

FIGURE 63.9: Centro-symmetric array configurations with a dual invariance structure: (a) URA with $M = 12$, $m_x = 9$, $m_y = 8$. (b) URFA with $M = 12$, $m_x = m_y = 6$. (c) Cross array with $M = 10$, $m_x = 3$, $m_y = 5$. (d) $M = 12$, $m_x = m_y = 7$.

Incident on the array are d narrowband planar wavefronts with wavelength λ, azimuth ϕ_i, and elevation θ_i, $1 \leq i \leq d$. Let

$$u_i = \cos\phi_i \sin\theta_i \quad \text{and} \quad v_i = \sin\phi_i \sin\theta_i, \quad 1 \leq i \leq d,$$

denote the direction cosines of the ith source relative to the x- and y-axes, respectively. These definitions are illustrated in Fig. 63.4. The fact that $\xi_i = u_i + \mathrm{j}v_i = \sin\theta_i\, e^{\mathrm{j}\phi_i}$ yields a simple formula

[8] In the examples of Fig. 63.9, all values of m_x and m_y correspond to selection matrices with maximum overlap in both directions. For a URA of $M = M_x \cdot M_y$ elements, cf. Fig. 63.9 (a), this assumption implies $m_x = (M_x - 1)\, M_y$ and $m_y = M_x\,(M_y - 1)$.

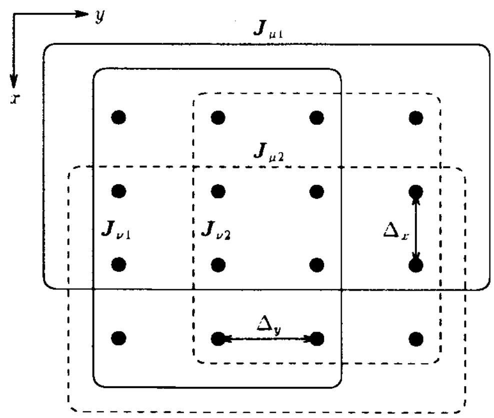

FIGURE 63.10: Subarray selection for a URA of $M = 4 \cdot 4 = 16$ sensor elements (maximum overlap in both directions: $m_x = m_y = 12$).

to determine azimuth ϕ_i and elevation θ_i from the corresponding direction cosines u_i and v_i, namely

$$\phi_i = \arg(\xi_i) \quad \text{and} \quad \theta_i = \arcsin(|\xi_i|), \quad \text{with} \quad \xi_i = u_i + \mathrm{j}v_i, \quad 1 \le i \le d. \tag{63.33}$$

Similar to the 1-D case, the data matrix $\boldsymbol{X}$ is an $M \times N$ matrix composed of N snapshots $\boldsymbol{x}(t_n)$, $1 \le n \le N$, of data as columns. Referring to Fig. 63.10 for a URA of $M = 4 \times 4 = 16$ sensors as an illustrative example, the antenna element outputs are stacked columnwise. Specifically, the first element of $\boldsymbol{x}(t_n)$ is the output of the antenna in the upper left corner. Then sequentially progress downwards along the positive x-axis such that the fourth element of $\boldsymbol{x}(t_n)$ is the output of the antenna in the bottom left corner. The fifth element of $\boldsymbol{x}(t_n)$ is the output of the antenna at the top of the second column; the eighth element of $\boldsymbol{x}(t_n)$ is the output of the antenna at the bottom of the second column, etc. This forms a 16×1 vector at each sampling instant t_n.

Similar to the 1-D case, the array measurements may be expressed as $\boldsymbol{x}(t) = \boldsymbol{A}\boldsymbol{s}(t) + \boldsymbol{n}(t) \in \mathbb{C}^M$. Due to the centro-symmetry of the array, the steering matrix $\boldsymbol{A} \in \mathbb{C}^{M \times d}$ satisfies Eq. (63.12). The goal is to construct two pairs of selection matrices that are centro-symmetric with respect to each other, i.e.,

$$\boldsymbol{J}_{\mu 2} = \boldsymbol{\Pi}_{m_x} \boldsymbol{J}_{\mu 1} \boldsymbol{\Pi}_M \quad \text{and} \quad \boldsymbol{J}_{\nu 2} = \boldsymbol{\Pi}_{m_y} \boldsymbol{J}_{\nu 1} \boldsymbol{\Pi}_M, \tag{63.34}$$

and cause the array steering matrix $\boldsymbol{A}$ to satisfy the following two invariance properties,

$$\boldsymbol{J}_{\mu 1} \boldsymbol{A} \boldsymbol{\Phi}_\mu = \boldsymbol{J}_{\mu 2} \boldsymbol{A} \qquad \text{and} \qquad \boldsymbol{J}_{\nu 1} \boldsymbol{A} \boldsymbol{\Phi}_\nu = \boldsymbol{J}_{\nu 2} \boldsymbol{A}, \tag{63.35}$$

where the diagonal matrices

$$\boldsymbol{\Phi}_\mu = \operatorname{diag}\left\{e^{\mathrm{j}\mu_i}\right\}_{i=1}^{d} \qquad \text{and} \qquad \boldsymbol{\Phi}_\nu = \operatorname{diag}\left\{e^{\mathrm{j}\nu_i}\right\}_{i=1}^{d} \tag{63.36}$$

are unitary and contain the desired 2-D angle information. Here $\mu_i = \frac{2\pi}{\lambda}\Delta_x u_i$ and $\nu_i = \frac{2\pi}{\lambda}\Delta_y v_i$ are the spatial frequencies in x- and y-direction, respectively.

Figure 63.10 visualizes a possible choice of the selection matrices for a URA of $M = 4 \times 4 = 16$ sensor elements. Given the stacking procedure described above and the 1-D selection matrices for a ULA of 4 elements

$$\boldsymbol{J}_1^{(4)} = \begin{bmatrix} 1 & 0 & 0 & 0 \\ 0 & 1 & 0 & 0 \\ 0 & 0 & 1 & 0 \end{bmatrix} \quad \text{and} \quad \boldsymbol{J}_2^{(4)} = \begin{bmatrix} 0 & 1 & 0 & 0 \\ 0 & 0 & 1 & 0 \\ 0 & 0 & 0 & 1 \end{bmatrix},$$

the appropriate selection matrices corresponding to maximum overlap are

$$\boldsymbol{J}_{\mu 1} = \boldsymbol{I}_{M_y} \otimes \boldsymbol{J}_1^{(M_x)} = \begin{bmatrix} 1 & 0 & 0 & 0 & 0 & 0 & 0 & 0 & 0 & 0 & 0 & 0 & 0 & 0 & 0 & 0 \\ 0 & 1 & 0 & 0 & 0 & 0 & 0 & 0 & 0 & 0 & 0 & 0 & 0 & 0 & 0 & 0 \\ 0 & 0 & 1 & 0 & 0 & 0 & 0 & 0 & 0 & 0 & 0 & 0 & 0 & 0 & 0 & 0 \\ 0 & 0 & 0 & 0 & 1 & 0 & 0 & 0 & 0 & 0 & 0 & 0 & 0 & 0 & 0 & 0 \\ 0 & 0 & 0 & 0 & 0 & 1 & 0 & 0 & 0 & 0 & 0 & 0 & 0 & 0 & 0 & 0 \\ 0 & 0 & 0 & 0 & 0 & 0 & 1 & 0 & 0 & 0 & 0 & 0 & 0 & 0 & 0 & 0 \\ 0 & 0 & 0 & 0 & 0 & 0 & 0 & 0 & 1 & 0 & 0 & 0 & 0 & 0 & 0 & 0 \\ 0 & 0 & 0 & 0 & 0 & 0 & 0 & 0 & 0 & 1 & 0 & 0 & 0 & 0 & 0 & 0 \\ 0 & 0 & 0 & 0 & 0 & 0 & 0 & 0 & 0 & 0 & 1 & 0 & 0 & 0 & 0 & 0 \\ 0 & 0 & 0 & 0 & 0 & 0 & 0 & 0 & 0 & 0 & 0 & 0 & 1 & 0 & 0 & 0 \\ 0 & 0 & 0 & 0 & 0 & 0 & 0 & 0 & 0 & 0 & 0 & 0 & 0 & 1 & 0 & 0 \\ 0 & 0 & 0 & 0 & 0 & 0 & 0 & 0 & 0 & 0 & 0 & 0 & 0 & 0 & 1 & 0 \end{bmatrix} \in \mathbb{R}^{12 \times 16}$$

$$\boldsymbol{J}_{\mu 2} = \boldsymbol{I}_{M_y} \otimes \boldsymbol{J}_2^{(M_x)} = \begin{bmatrix} 0 & 1 & 0 & 0 & 0 & 0 & 0 & 0 & 0 & 0 & 0 & 0 & 0 & 0 & 0 & 0 \\ 0 & 0 & 1 & 0 & 0 & 0 & 0 & 0 & 0 & 0 & 0 & 0 & 0 & 0 & 0 & 0 \\ 0 & 0 & 0 & 1 & 0 & 0 & 0 & 0 & 0 & 0 & 0 & 0 & 0 & 0 & 0 & 0 \\ 0 & 0 & 0 & 0 & 0 & 1 & 0 & 0 & 0 & 0 & 0 & 0 & 0 & 0 & 0 & 0 \\ 0 & 0 & 0 & 0 & 0 & 0 & 1 & 0 & 0 & 0 & 0 & 0 & 0 & 0 & 0 & 0 \\ 0 & 0 & 0 & 0 & 0 & 0 & 0 & 1 & 0 & 0 & 0 & 0 & 0 & 0 & 0 & 0 \\ 0 & 0 & 0 & 0 & 0 & 0 & 0 & 0 & 0 & 1 & 0 & 0 & 0 & 0 & 0 & 0 \\ 0 & 0 & 0 & 0 & 0 & 0 & 0 & 0 & 0 & 0 & 1 & 0 & 0 & 0 & 0 & 0 \\ 0 & 0 & 0 & 0 & 0 & 0 & 0 & 0 & 0 & 0 & 0 & 1 & 0 & 0 & 0 & 0 \\ 0 & 0 & 0 & 0 & 0 & 0 & 0 & 0 & 0 & 0 & 0 & 0 & 0 & 1 & 0 & 0 \\ 0 & 0 & 0 & 0 & 0 & 0 & 0 & 0 & 0 & 0 & 0 & 0 & 0 & 0 & 1 & 0 \\ 0 & 0 & 0 & 0 & 0 & 0 & 0 & 0 & 0 & 0 & 0 & 0 & 0 & 0 & 0 & 1 \end{bmatrix} \in \mathbb{R}^{12 \times 16}$$

$$\boldsymbol{J}_{\nu 1} = \boldsymbol{J}_1^{(M_y)} \otimes \boldsymbol{I}_{M_x} = \begin{bmatrix} 1 & 0 & 0 & 0 & 0 & 0 & 0 & 0 & 0 & 0 & 0 & 0 & 0 & 0 & 0 & 0 \\ 0 & 1 & 0 & 0 & 0 & 0 & 0 & 0 & 0 & 0 & 0 & 0 & 0 & 0 & 0 & 0 \\ 0 & 0 & 1 & 0 & 0 & 0 & 0 & 0 & 0 & 0 & 0 & 0 & 0 & 0 & 0 & 0 \\ 0 & 0 & 0 & 1 & 0 & 0 & 0 & 0 & 0 & 0 & 0 & 0 & 0 & 0 & 0 & 0 \\ 0 & 0 & 0 & 0 & 1 & 0 & 0 & 0 & 0 & 0 & 0 & 0 & 0 & 0 & 0 & 0 \\ 0 & 0 & 0 & 0 & 0 & 1 & 0 & 0 & 0 & 0 & 0 & 0 & 0 & 0 & 0 & 0 \\ 0 & 0 & 0 & 0 & 0 & 0 & 1 & 0 & 0 & 0 & 0 & 0 & 0 & 0 & 0 & 0 \\ 0 & 0 & 0 & 0 & 0 & 0 & 0 & 1 & 0 & 0 & 0 & 0 & 0 & 0 & 0 & 0 \\ 0 & 0 & 0 & 0 & 0 & 0 & 0 & 0 & 1 & 0 & 0 & 0 & 0 & 0 & 0 & 0 \\ 0 & 0 & 0 & 0 & 0 & 0 & 0 & 0 & 0 & 1 & 0 & 0 & 0 & 0 & 0 & 0 \\ 0 & 0 & 0 & 0 & 0 & 0 & 0 & 0 & 0 & 0 & 1 & 0 & 0 & 0 & 0 & 0 \\ 0 & 0 & 0 & 0 & 0 & 0 & 0 & 0 & 0 & 0 & 0 & 1 & 0 & 0 & 0 & 0 \end{bmatrix} \in \mathbb{R}^{12 \times 16}$$

$$
\boldsymbol{J}_{\nu 2} = \boldsymbol{J}_2^{(M_y)} \otimes \boldsymbol{I}_{M_x} = \begin{bmatrix}
0&0&0&0&1&0&0&0&0&0&0&0&0&0&0&0\\
0&0&0&0&0&1&0&0&0&0&0&0&0&0&0&0\\
0&0&0&0&0&0&1&0&0&0&0&0&0&0&0&0\\
0&0&0&0&0&0&0&1&0&0&0&0&0&0&0&0\\
0&0&0&0&0&0&0&0&1&0&0&0&0&0&0&0\\
0&0&0&0&0&0&0&0&0&1&0&0&0&0&0&0\\
0&0&0&0&0&0&0&0&0&0&1&0&0&0&0&0\\
0&0&0&0&0&0&0&0&0&0&0&1&0&0&0&0\\
0&0&0&0&0&0&0&0&0&0&0&0&1&0&0&0\\
0&0&0&0&0&0&0&0&0&0&0&0&0&1&0&0\\
0&0&0&0&0&0&0&0&0&0&0&0&0&0&1&0\\
0&0&0&0&0&0&0&0&0&0&0&0&0&0&0&1
\end{bmatrix} \in \mathbb{R}^{12\times 16},
$$

where $M_x = M_y = 4$. Notice, however, that it is not required to compute all four selection matrices explicitly, since they are related via Eq. (63.34). In fact, to be able to compute the four transformed selection matrices for 2-D Unitary ESPRIT, it is sufficient to specify $\boldsymbol{J}_{\mu 2}$ and $\boldsymbol{J}_{\nu 2}$, cf. (63.38) and (63.39).

63.6.2 2-D Unitary ESPRIT in Element Space

Similar to Eq. (63.16) in the 1-D case, let us define the transformed 2-D array steering matrix as $\boldsymbol{D} = \boldsymbol{Q}_M^H \boldsymbol{A}$. Based on the two invariance properties of the 2-D array steering matrix $\boldsymbol{A}$ in Eq. (63.35), it is a straightforward 2-D extension of the derivation of 1-D Unitary ESPRIT to show that the transformed array steering matrix $\boldsymbol{D}$ satisfies

$$
\boldsymbol{K}_{\mu 1}\boldsymbol{D} \cdot \boldsymbol{\Omega}_\mu = \boldsymbol{K}_{\mu 2}\boldsymbol{D} \qquad \text{and} \qquad \boldsymbol{K}_{\nu 1}\boldsymbol{D} \cdot \boldsymbol{\Omega}_\nu = \boldsymbol{K}_{\nu 2}\boldsymbol{D}, \tag{63.37}
$$

where the two pairs of transformed selection matrices are defined as

$$
\boldsymbol{K}_{\mu 1} = 2 \cdot \mathrm{Re}\{\boldsymbol{Q}_{m_x}^H \boldsymbol{J}_{\mu 2}\, \boldsymbol{Q}_M\} \qquad \boldsymbol{K}_{\mu 2} = 2 \cdot \mathrm{Im}\{\boldsymbol{Q}_{m_x}^H \boldsymbol{J}_{\mu 2}\, \boldsymbol{Q}_M\} \tag{63.38}
$$

$$
\boldsymbol{K}_{\nu 1} = 2 \cdot \mathrm{Re}\{\boldsymbol{Q}_{m_y}^H \boldsymbol{J}_{\nu 2}\, \boldsymbol{Q}_M\} \qquad \boldsymbol{K}_{\nu 2} = 2 \cdot \mathrm{Im}\{\boldsymbol{Q}_{m_y}^H \boldsymbol{J}_{\nu 2}\, \boldsymbol{Q}_M\} \tag{63.39}
$$

and the real-valued diagonal matrices

$$
\boldsymbol{\Omega}_\mu = \mathrm{diag}\left\{\tan\left(\frac{\mu_i}{2}\right)\right\}_{i=1}^d \qquad \text{and} \qquad \boldsymbol{\Omega}_\nu = \mathrm{diag}\left\{\tan\left(\frac{\nu_i}{2}\right)\right\}_{i=1}^d \tag{63.40}
$$

contain the desired (spatial) frequency information.

Given the noise-corrupted data matrix $\boldsymbol{X}$, a real-valued matrix $\boldsymbol{E}_s$, spanning the dominant subspace of $\mathcal{T}(\boldsymbol{X})$, is obtained as described in Section 63.3.1 for the 1-D case. Asymptotically or without additive noise, $\boldsymbol{E}_s$ and $\boldsymbol{D}$ span the same d-dimensional subspace, i.e., there is a nonsingular matrix $\boldsymbol{T}$ of size $d \times d$ such that $\boldsymbol{D} \approx \boldsymbol{E}_s\boldsymbol{T}$. Substituting this relationship into Eq. (63.37) yields two *real-valued* invariance equations

$$
\boldsymbol{K}_{\mu 1}\boldsymbol{E}_s\boldsymbol{\Upsilon}_\mu \approx \boldsymbol{K}_{\mu 2}\boldsymbol{E}_s \in \mathbb{R}^{m_x \times d} \qquad \text{and} \qquad \boldsymbol{K}_{\nu 1}\boldsymbol{E}_s\boldsymbol{\Upsilon}_\nu \approx \boldsymbol{K}_{\nu 2}\boldsymbol{E}_s \in \mathbb{R}^{m_y \times d}, \tag{63.41}
$$

where $\boldsymbol{\Upsilon}_\mu = \boldsymbol{T}\,\boldsymbol{\Omega}_\mu\,\boldsymbol{T}^{-1} \in \mathbb{R}^{d\times d}$ and $\boldsymbol{\Upsilon}_\nu = \boldsymbol{T}\,\boldsymbol{\Omega}_\nu\,\boldsymbol{T}^{-1} \in \mathbb{R}^{d\times d}$. Thus, $\boldsymbol{\Upsilon}_\mu$ and $\boldsymbol{\Upsilon}_\nu$ are related with the diagonal matrices $\boldsymbol{\Omega}_\mu$ and $\boldsymbol{\Omega}_\nu$ via eigenvalue preserving similarity transformations. Moreover, the real-valued matrices $\boldsymbol{\Upsilon}_\mu$ and $\boldsymbol{\Upsilon}_\nu$ share the *same set of eigenvectors*. As in the 1-D case, the two real-valued invariance equations (63.41) can be solved independently via LS, TLS, or SLS [9]. As an alternative, they may be solved jointly via 2-D SLS, which is a 2-D extension of structured least squares (SLS) [8].

63.6.3 Automatic Pairing of the 2-D Frequency Estimates

Asymptotically or without additive noise, the real-valued eigenvalues of the solutions $\boldsymbol{\Upsilon}_\mu \in \mathbb{R}^{d\times d}$ and $\boldsymbol{\Upsilon}_\nu \in \mathbb{R}^{d\times d}$ to the invariance equations above are given by $\tan(\mu_i/2)$ and $\tan(\nu_i/2)$, respectively. If theses eigenvalues were calculated independently, it would be quite difficult to pair the resulting two distinct sets of frequency estimates. Notice that one can choose a real-valued eigenvector matrix $\boldsymbol{T}$ such that all matrices that appear in the spectral decompositions of $\boldsymbol{\Upsilon}_\mu = \boldsymbol{T}\,\boldsymbol{\Omega}_\mu\,\boldsymbol{T}^{-1}$ and $\boldsymbol{\Upsilon}_\nu = \boldsymbol{T}\,\boldsymbol{\Omega}_\nu\,\boldsymbol{T}^{-1}$ are real-valued. Moreover, the subspace spanned by the columns of $\boldsymbol{T} \in \mathbb{R}^{d\times d}$ is unique. These observations are critical to achieve automatic pairing of the spatial frequencies μ_i and ν_i, $1 \le i \le d$.

With additive noise and a finite number of snapshots N, however, the real-valued matrices $\boldsymbol{\Upsilon}_\mu$ and $\boldsymbol{\Upsilon}_\nu$ do not exactly share the same set of eigenvectors. To determine an approximation of the set of common eigenvectors from one of these matrices is, obviously, not the best solution, since this strategy would rely on an arbitrary choice and would also discard information contained in the other matrix. Moreover, $\boldsymbol{\Upsilon}_\mu$ and $\boldsymbol{\Upsilon}_\nu$ might have some degenerate (multiple) eigenvalues, while both of them have well determined common eigenvectors $\boldsymbol{T}$ (for $N \to \infty$ or $\sigma_N^2 \to 0$). 2-D Unitary ESPRIT circumvents these difficulties and achieves automatic pairing of the spatial frequency estimates μ_i and ν_i by computing the eigenvalues of the "complexified" matrix $\boldsymbol{\Upsilon}_\mu + \mathrm{j}\,\boldsymbol{\Upsilon}_\nu$ since this complex-valued matrix may be spectrally decomposed as

$$\boldsymbol{\Upsilon}_\mu + \mathrm{j}\,\boldsymbol{\Upsilon}_\nu = \boldsymbol{T}\left(\boldsymbol{\Omega}_\mu + \mathrm{j}\,\boldsymbol{\Omega}_\nu\right)\boldsymbol{T}^{-1}. \tag{63.42}$$

Here, automatically paired estimates of $\boldsymbol{\Omega}_\mu$ and $\boldsymbol{\Omega}_\nu$ in Eq. (63.40) are given by the real and imaginary parts of the complex eigenvalues of $\boldsymbol{\Upsilon}_\mu + \mathrm{j}\,\boldsymbol{\Upsilon}_\nu$. The maximum number of sources 2-D Unitary ESPRIT can handle is the minimum of m_x and m_y, assuming that at least $d/2$ snapshots are available. If only a single snapshot is available (or more than two sources are highly correlated), one can extract $d/2$ or more identical subarrays out of the overall array to get the effect of multiple snapshots (spatial smoothing), thereby decreasing the maximum number of sources that can be handled. A brief summary of the described element space implementation of 2-D Unitary ESPRIT is given in Table 63.6.

TABLE 63.6 Summary of 2-D Unitary ESPRIT in Element Space

1. *Signal Subspace Estimation:* Compute $\boldsymbol{E}_s \in \mathbb{R}^{M\times d}$ as the d dominant left singular vectors of $\mathcal{T}(\boldsymbol{X}) \in \mathbb{R}^{M\times 2N}$.
2. *Solution of the Invariance Equations:* Solve

$$\underbrace{\boldsymbol{K}_{\mu 1}\boldsymbol{E}_s}_{\mathbb{R}^{m_x\times d}}\boldsymbol{\Upsilon}_\mu \approx \underbrace{\boldsymbol{K}_{\mu 2}\boldsymbol{E}_s}_{\mathbb{R}^{m_x\times d}} \quad \text{and} \quad \underbrace{\boldsymbol{K}_{\nu 1}\boldsymbol{E}_s}_{\mathbb{R}^{m_y\times d}}\boldsymbol{\Upsilon}_\nu \approx \underbrace{\boldsymbol{K}_{\nu 2}\boldsymbol{E}_s}_{\mathbb{R}^{m_y\times d}}$$

   by means of LS, TLS, SLS, or 2-D SLS.
3. *Spatial Frequency Estimation:* Calculate the eigenvalues of the complex-valued $d\times d$ matrix

$$\boldsymbol{\Upsilon}_\mu + \mathrm{j}\,\boldsymbol{\Upsilon}_\nu = \boldsymbol{T}\,\boldsymbol{\Lambda}\,\boldsymbol{T}^{-1} \quad \text{with} \quad \boldsymbol{\Lambda} = \mathrm{diag}\,\{\lambda_i\}_{i=1}^d$$

   - $\mu_i = 2\arctan\left(\mathrm{Re}\,\{\lambda_i\}\right), \qquad 1 \le i \le d$
   - $\nu_i = 2\arctan\left(\mathrm{Im}\,\{\lambda_i\}\right), \qquad 1 \le i \le d$

It is instructive to examine a very simple numerical example. Consider a uniform rectangular array (URA) of $M = 2\times 2 = 4$ sensor elements, i.e., $M_x = M_y = 2$. Effecting maximum overlap, we have $m_x = m_y = 2$. For the sake of simplicity, assume that the true covariance matrix of the noise-corrupted measurements

$$\boldsymbol{R}_{xx} = \mathrm{E}\{\boldsymbol{x}(t)\boldsymbol{x}^H(t)\} = \boldsymbol{A}\boldsymbol{R}_{ss}\boldsymbol{A}^H + \sigma_N^2 \boldsymbol{I}_4 = \begin{bmatrix} 3 & 0 & 1-\mathrm{j} & -1+\mathrm{j} \\ 0 & 3 & 1-\mathrm{j} & 1-\mathrm{j} \\ 1+\mathrm{j} & 1+\mathrm{j} & 3 & 0 \\ -1-\mathrm{j} & 1+\mathrm{j} & 0 & 3 \end{bmatrix}$$

is known. Here, $\boldsymbol{R}_{ss} = \mathrm{E}\{\boldsymbol{s}(t)\boldsymbol{s}^H(t)\} \in \mathbb{C}^{d\times d}$ denotes the unknown signal covariance matrix. Furthermore, the measurement vector $\boldsymbol{x}(t)$ is defined as

$$\boldsymbol{x}(t) = \begin{bmatrix} x_{11}(t) & x_{12}(t) & x_{21}(t) & x_{22}(t) \end{bmatrix}^T . \tag{63.43}$$

In this example, we have to use a covariance approach instead of the direct data approach summarized in Table 63.6, since the array measurements $\boldsymbol{x}(t)$ themselves are not known. To this end, we will compute the eigendecomposition of the real part of the transformed covariance matrix as, for instance, discussed in [25]. According to Eq. (63.13), the left $\boldsymbol{\Pi}$-real transformation matrices $\boldsymbol{Q}_M$ and $\boldsymbol{Q}_{m_x} = \boldsymbol{Q}_{m_y}$ take the form

$$\boldsymbol{Q}_4 = \frac{1}{\sqrt{2}} \begin{bmatrix} 1 & 0 & \mathrm{j} & 0 \\ 0 & 1 & 0 & \mathrm{j} \\ 0 & 1 & 0 & -\mathrm{j} \\ 1 & 0 & -\mathrm{j} & 0 \end{bmatrix} \quad \text{and} \quad \boldsymbol{Q}_2 = \frac{1}{\sqrt{2}} \begin{bmatrix} 1 & \mathrm{j} \\ 1 & -\mathrm{j} \end{bmatrix},$$

respectively. Therefore, we have

$$\boldsymbol{R}_Q = \mathrm{Re}\left\{\boldsymbol{Q}_4^H \boldsymbol{R}_{xx} \boldsymbol{Q}_4\right\} = \boldsymbol{Q}_4^H \boldsymbol{R}_{xx} \boldsymbol{Q}_4 = \begin{bmatrix} 2 & 1 & 1 & -1 \\ 1 & 4 & -1 & -1 \\ 1 & -1 & 4 & -1 \\ -1 & -1 & -1 & 2 \end{bmatrix} . \tag{63.44}$$

The eigenvalues of $\boldsymbol{R}_Q$ are given by $\varrho_1 = 5$, $\varrho_2 = 5$, $\varrho_3 = 1$, and $\varrho_4 = 1$. Clearly, ϱ_1 and ϱ_2 are the dominant eigenvalues, and the variance of the additive noise is identified as $\sigma_N^2 = \varrho_3 = \varrho_4 = 1$. Therefore, there are $d = 2$ impinging wavefronts. The columns of

$$\boldsymbol{E}_s = \begin{bmatrix} 1 & 0 \\ 1 & 1 \\ 1 & -1 \\ -1 & 0 \end{bmatrix}$$

contain eigenvectors of $\boldsymbol{R}_Q$ corresponding to the $d = 2$ largest eigenvalues ϱ_1 and ϱ_2. The four selection matrices

$$\begin{aligned} \boldsymbol{J}_{\mu 1} &= \begin{bmatrix} 1 & 0 & 0 & 0 \\ 0 & 0 & 1 & 0 \end{bmatrix}, \; \boldsymbol{J}_{\mu 2} = \begin{bmatrix} 0 & 1 & 0 & 0 \\ 0 & 0 & 0 & 1 \end{bmatrix}, \\ \boldsymbol{J}_{\nu 1} &= \begin{bmatrix} 1 & 0 & 0 & 0 \\ 0 & 1 & 0 & 0 \end{bmatrix}, \; \boldsymbol{J}_{\nu 2} = \begin{bmatrix} 0 & 0 & 1 & 0 \\ 0 & 0 & 0 & 1 \end{bmatrix}, \end{aligned}$$

are constructed in accordance with Eq. (63.43), cf. Fig. 63.10, yielding

$$\begin{aligned} \boldsymbol{K}_{\mu 1} &= \begin{bmatrix} 1 & 1 & 0 & 0 \\ 0 & 0 & 1 & 1 \end{bmatrix}, & \boldsymbol{K}_{\mu 2} &= \begin{bmatrix} 0 & 0 & -1 & 1 \\ 1 & -1 & 0 & 0 \end{bmatrix}, \\ \boldsymbol{K}_{\nu 1} &= \begin{bmatrix} 1 & 1 & 0 & 0 \\ 0 & 0 & 1 & -1 \end{bmatrix}, & \boldsymbol{K}_{\nu 2} &= \begin{bmatrix} 0 & 0 & -1 & -1 \\ 1 & -1 & 0 & 0 \end{bmatrix}, \end{aligned}$$

according to Eq. (63.38) and Eq. (63.39). With these definitions, the invariance equations (63.41) turn out to be

$$\begin{bmatrix} 2 & 1 \\ 0 & -1 \end{bmatrix} \boldsymbol{\Upsilon}_\mu \approx \begin{bmatrix} -2 & 1 \\ 0 & -1 \end{bmatrix} \quad \text{and} \quad \begin{bmatrix} 2 & 1 \\ 2 & -1 \end{bmatrix} \boldsymbol{\Upsilon}_\nu \approx \begin{bmatrix} 0 & 1 \\ 0 & -1 \end{bmatrix}.$$

Solving these matrix equations, we get

$$\boldsymbol{\Upsilon}_\mu = \begin{bmatrix} -1 & 0 \\ 0 & 1 \end{bmatrix} \quad \text{and} \quad \boldsymbol{\Upsilon}_\nu = \begin{bmatrix} 0 & 0 \\ 0 & 1 \end{bmatrix}.$$

Finally, the eigenvalues of the "complexified" 2×2 matrix $\boldsymbol{\Upsilon}_\mu + \mathrm{j}\boldsymbol{\Upsilon}_\nu$ are observed to be $\lambda_1 = -1$ and $\lambda_2 = 1 + \mathrm{j}$, corresponding to the spatial frequencies

$$\mu_1 = -\frac{\pi}{2}, \quad \nu_1 = 0 \quad \text{and} \quad \mu_2 = \frac{\pi}{2}, \quad \nu_2 = \frac{\pi}{2}.$$

If we assume that $\Delta_x = \Delta_y = \lambda/2$, the direction cosines are given by $u_i = \mu_i/\pi$ and $v_i = \nu_i/\pi$, $i = 1, 2$. According to Eq. (63.33), the corresponding azimuth and elevation angles can be calculated as

$$\phi_1 = 180^\circ, \quad \theta_1 = 30^\circ, \quad \text{and} \quad \phi_2 = 45^\circ, \quad \theta_2 = 45^\circ.$$

63.6.4 2-D Unitary ESPRIT in DFT Beamspace

Here, we will restrict the presentation of 2-D Unitary ESPRIT in DFT beamspace to uniform rectangular arrays (URAs) of $M = M_x \cdot M_y$ identical sensors, cf. Fig. 63.10.[9] Without loss of generality, assume that the M sensors are omnidirectional and that the centroid of the URA is chosen as the phase reference.

Let us form B_x out of M_x beams in x-direction and B_y out of M_y beams in y-direction, yielding a total of $B = B_x \cdot B_y$ beams. Then the corresponding scaled DFT-matrices $\boldsymbol{W}_{B_x}^H \in \mathbb{C}^{B_x \times M_x}$ and $\boldsymbol{W}_{B_y}^H \in \mathbb{C}^{B_y \times M_y}$ are formed as discussed in Section 63.3.2. Now, viewing the array output at a given snapshot as an $M_x \times M_y$ matrix, premultiply this matrix by $\boldsymbol{W}_{B_x}^H$ and postmultiply it by $\overline{\boldsymbol{W}}_{B_y}$.[10] Then apply the vec$\{\cdot\}$-operator, and place the resulting $B \times 1$ vector ($B = B_x \cdot B_y$) as a column of a matrix $\boldsymbol{Y} \in \mathbb{C}^{B \times N}$. The vec$\{\cdot\}$-operator maps a $B_x \times B_y$ matrix to a $B \times 1$ vector by stacking the columns of the matrix. Note that if $\boldsymbol{X}$ denotes the $M \times N$ complex-valued element space data matrix, it is easy to show that the relationship between $\boldsymbol{Y}$ and $\boldsymbol{X}$ may be expressed as $\boldsymbol{Y} = (\boldsymbol{W}_{B_y}^H \otimes \boldsymbol{W}_{B_x}^H)\boldsymbol{X}$ [24]. Here, the symbol $\otimes$ denotes the Kronecker matrix product [5].

Let the columns of $\boldsymbol{E}_s \in \mathbb{R}^{B \times d}$ contain the d left singular vectors of

$$\begin{bmatrix} \mathrm{Re}\{\boldsymbol{Y}\} & \mathrm{Im}\{\boldsymbol{Y}\} \end{bmatrix} \in \mathbb{R}^{B \times 2N} \tag{63.45}$$

corresponding to its d largest singular values. To set up two invariance equations similar to Eq. (63.41), but with a reduced dimensionality, let us define the selection matrices

$$\boldsymbol{\Gamma}_{\mu 1} = \boldsymbol{I}_{B_y} \otimes \boldsymbol{\Gamma}_1^{(B_x)} \quad \text{and} \quad \boldsymbol{\Gamma}_{\mu 2} = \boldsymbol{I}_{B_y} \otimes \boldsymbol{\Gamma}_2^{(B_x)} \tag{63.46}$$

[9] In [24], we have also described how to use 2-D Unitary ESPRIT in DFT beamspace for cross arrays as depicted in Fig. 63.9 (c).

[10] This can be achieved via a 2-D FFT with appropriate scaling.

of size $b_x \times B$ for the x-direction ($b_x = (B_x - 1) \cdot B_y$) and

$$\boldsymbol{\Gamma}_{\nu 1} = \boldsymbol{\Gamma}_1^{(B_y)} \otimes \boldsymbol{I}_{B_x} \quad \text{and} \quad \boldsymbol{\Gamma}_{\nu 2} = \boldsymbol{\Gamma}_2^{(B_y)} \otimes \boldsymbol{I}_{B_x} \tag{63.47}$$

of size $b_y \times B$ for the y-direction ($b_y = B_x \cdot (B_y - 1)$). Then $\boldsymbol{\Upsilon}_\mu \in \mathbb{R}^{d \times d}$ and $\boldsymbol{\Upsilon}_\nu \in \mathbb{R}^{d \times d}$ can be calculated as the LS, TLS, SLS, or 2-D SLS solution of

$$\boldsymbol{\Gamma}_{\mu 1} \boldsymbol{E}_s \boldsymbol{\Upsilon}_\mu \approx \boldsymbol{\Gamma}_{\mu 2} \boldsymbol{E}_s \in \mathbb{R}^{b_x \times d} \quad \text{and} \quad \boldsymbol{\Gamma}_{\nu 1} \boldsymbol{E}_s \boldsymbol{\Upsilon}_\nu \approx \boldsymbol{\Gamma}_{\nu 2} \boldsymbol{E}_s \in \mathbb{R}^{b_y \times d}, \tag{63.48}$$

respectively. Finally, the desired *automatically paired* spatial frequency estimates μ_i and ν_i, $1 \leq i \leq d$, are obtained from the real and imaginary part of the eigenvalues of the "complexified" matrix $\boldsymbol{\Upsilon}_\mu + \mathrm{j}\boldsymbol{\Upsilon}_\nu$ as discussed in Section 63.6.2. Here, the maximum number of sources we can handle is given by the minimum of b_x and b_y, assuming that at least $d/2$ snapshots are available. A summary of 2-D Unitary ESPRIT in DFT beamspace is presented in Table 63.7.

TABLE 63.7 Summary of 2-D Unitary ESPRIT in DFT Beamspace

0. *Transformation to Beamspace:* Compute a 2-D DFT (with appropriate scaling) of the $M_x \times M_y$ matrix of array outputs at each snapshot, apply the vec$\{\cdot\}$-operator, and place the result as a column of $\boldsymbol{Y} \implies \boldsymbol{Y} = \left(\boldsymbol{W}_{B_y}^H \otimes \boldsymbol{W}_{B_x}^H\right) \boldsymbol{X} \in \mathbb{C}^{B \times N}$ $(B = B_x \cdot B_y)$.

1. *Signal Subspace Estimation:* Compute $\boldsymbol{E}_s \in \mathbb{R}^{B \times d}$ as the d dominant left singular vectors of $\begin{bmatrix} \mathrm{Re}\{\boldsymbol{Y}\} & \mathrm{Im}\{\boldsymbol{Y}\} \end{bmatrix} \in \mathbb{R}^{B \times 2N}$.

2. *Solution of the Invariance Equations:* Solve

$$\underbrace{\boldsymbol{\Gamma}_{\mu 1} \boldsymbol{E}_s}_{\mathbb{R}^{b_x \times d}} \boldsymbol{\Upsilon}_\mu \approx \underbrace{\boldsymbol{\Gamma}_{\mu 2} \boldsymbol{E}_s}_{\mathbb{R}^{b_x \times d}} \quad \text{and} \quad \underbrace{\boldsymbol{\Gamma}_{\nu 1} \boldsymbol{E}_s}_{\mathbb{R}^{b_y \times d}} \boldsymbol{\Upsilon}_\nu \approx \underbrace{\boldsymbol{\Gamma}_{\nu 2} \boldsymbol{E}_s}_{\mathbb{R}^{b_y \times d}}$$
$$b_x = (B_x - 1) \cdot B_y \qquad\qquad b_y = B_x \cdot (B_y - 1)$$

by means of LS, TLS, SLS, or 2-D SLS.

3. *Spatial Frequency Estimation:* Calculate the eigenvalues of the complex-valued $d \times d$ matrix

$$\boldsymbol{\Upsilon}_\mu + \mathrm{j}\boldsymbol{\Upsilon}_\nu = \boldsymbol{T} \boldsymbol{\Lambda} \boldsymbol{T}^{-1} \quad \text{with} \quad \boldsymbol{\Lambda} = \mathrm{diag}\,\{\lambda_i\}_{i=1}^d$$

- $\mu_i = 2 \arctan\left(\mathrm{Re}\left\{\lambda_i\right\}\right), \qquad 1 \leq i \leq d$
- $\nu_i = 2 \arctan\left(\mathrm{Im}\left\{\lambda_i\right\}\right), \qquad 1 \leq i \leq d$

63.6.5 Simulation Results

Simulations were conducted employing a URA of 8×8 elements, i.e., $M_x = M_y = 8$, with $\Delta_x = \Delta_y = \lambda/2$. The source scenario consisted of $d = 3$ equi-powered, uncorrelated sources located at $(u_1, v_1) = (0, 0)$, $(u_2, v_2) = (1/8, 0)$, and $(u_3, v_3) = (0, 1/8)$, where u_i and v_i are the direction cosines of the ith source relative to the x- and y-axes, respectively. Notice that sources 1 and 2 have the same v-coordinates, while sources 2 and 3 have the same u-coordinates. A given trial run at a given SNR level (per source per element) involved $N = 64$ snapshots. The noise was *i.i.d.* from element to element and from snapshot to snapshot. The RMS error defined as

$$\mathrm{RMSE}_i = \sqrt{\mathrm{E}\{(\hat{u}_i - u_i)^2\} + \mathrm{E}\{(\hat{v}_i - v_i)^2\}}, \quad i = 1, 2, 3, \tag{63.49}$$

was employed as the performance metric. Let $(\hat{u}_{i_k}, \hat{v}_{i_k})$ denote the coordinate estimates of the ith source obtained at the kth run. Sample performance statistics were computed from $K = 1000$

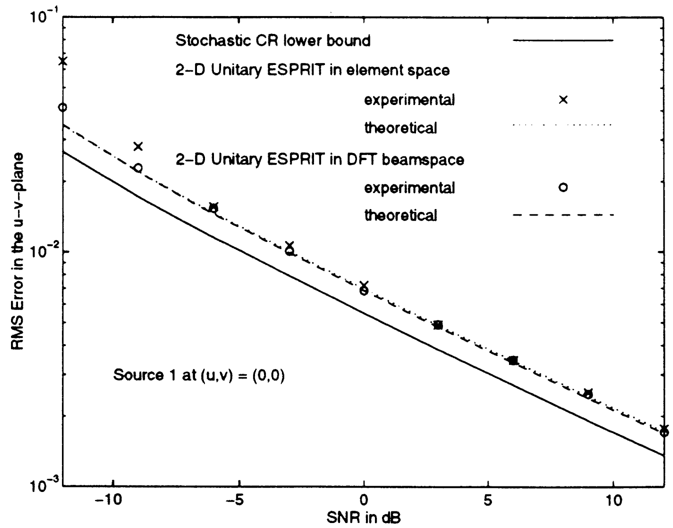

FIGURE 63.11: RMS error of source 1 at $(u_1, v_1) = (0, 0)$ in the u-v plane as a function of the SNR (8×8 sensors, $N = 64$, 1000 trial runs).

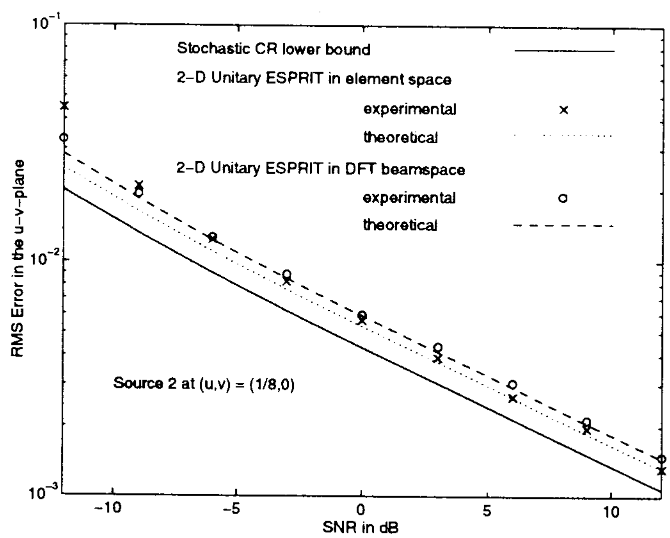

FIGURE 63.12: RMS error of source 2 at $(u_2, v_2) = (1/8, 0)$ in the u-v plane as a function of the SNR (8×8 sensors, $N = 64$, 1000 trial runs).

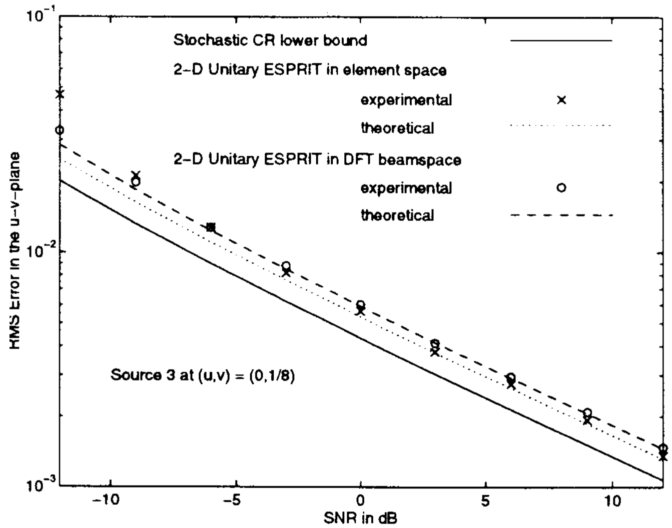

FIGURE 63.13: RMS error of source 3 at $(u_3, v_3) = (0, 1/8)$ in the u-v plane as a function of the SNR (8×8 sensors, $N = 64$, 1000 trial runs).

independent trials as

$$\widehat{\mathrm{RMSE}}_i = \sqrt{\frac{1}{K}\sum_{k=1}^{T}\left\{(\hat{u}_{i_k} - u_i)^2 + (\hat{v}_{i_k} - v_i)^2\right\}}, \quad i = 1, 2, 3. \tag{63.50}$$

2-D Unitary ESPRIT in DFT beamspace was implemented with a set of $B = 9$ beams centered at $(u, v) = (0, 0)$, using $B_x = 3$ out of $M_x = 8$ in x-direction (rows 8, 1, and 2 of $\boldsymbol{W}_8^H$) and also $B_y = 3$ out of $M_y = 8$ in y-direction (again, rows 8, 1, and 2 of $\boldsymbol{W}_8^H$). Thus, the corresponding subblocks of the selection matrices $\boldsymbol{\Gamma}_1 \in \mathbb{R}^{8\times 8}$ and $\boldsymbol{\Gamma}_2 \in \mathbb{R}^{8\times 8}$, used to form $\boldsymbol{\Gamma}_1^{(B_x)}$ and $\boldsymbol{\Gamma}_2^{(B_x)}$ in Eq. (63.46) and also used to form $\boldsymbol{\Gamma}_1^{(B_y)}$ and $\boldsymbol{\Gamma}_2^{(B_y)}$ in Eq. (63.47), are shaded in Fig. 63.3 (b). The bias of 2-D Unitary ESPRIT in element space and DFT beamspace was found to be negligible, facilitating comparison with the Cramér-Rao (CR) lower bound [15]. The resulting performance curves are plotted in Figs. 63.11, 63.12, and 63.13. We have also included theoretical performance predictions of both implementations based on an asymptotic performance analysis [13, 14]. Observe that the empirical RMSEs closely follow the theoretical predictions, except for deviations at low SNRs. The performance of the DFT beamspace implementation is comparable to that of the element space implementation. However, the former requires significantly less computations than the latter, since it operates in a $B = B_x \cdot B_y = 9$ dimensional beamspace as opposed to an $M = M_x \cdot M_y = 64$ dimensional element space.

For SNRs lower than −9 dB, the DFT beamspace version outperformed the element space version of 2-D Unitary ESPRIT. This is due to fact that the DFT beamspace version exploits *a priori* information on the source locations by forming beams pointed in the general directions of the sources.

References

[1] Bienvenu, G. and Kopp, L., Decreasing high resolution method sensitivity by conventional beamforming preprocessing, *Proc. IEEE Int. Conf. Acoust., Speech, Signal Processing,* 33.2.1–33.2.4, San Diego, CA, Mar. 1984.

[2] Brennan, P.V., A low cost phased array antenna for land-mobile satcom applications, *IEEE Proceedings-H*, 138, 131–136, Apr. 1991.

[3] Buckley, K.M. and Xu, X.L., Spatial-spectrum estimation in a location sector, *IEEE Trans. Acoust., Speech, Signal Processing,* ASSP-38, 1842–1852, Nov. 1990.

[4] Davies, D.E.N., *The Handbook of Antenna Design*, vol. 2, Peter Peregrinus, London, U.K., 1983, chap. 12.

[5] Graham, A., *Kronecker Products and Matrix Calculus: With Applications*, Ellis Horwood, Chichester, U.K., 1981.

[6] Haardt, M., Hüper, K., Moore, J.B. and Nossek, J.A., Simultaneous Schur decomposition of several matrices to achieve automatic pairing in multidimensional harmonic retrieval problems, in *Signal Processing VIII: Theories and Applications (Proc. of EUSIPCO-96),* Trieste, Italy, Sept. 1996, European Association for Signal Processing.

[7] Haardt, M. and Nossek, J.A., Unitary ESPRIT: How to obtain increased estimation accuracy with a reduced computational burden, *IEEE Trans. Signal Processing,* 43, 1232–1242, May 1995.

[8] Haardt, M. and Nossek, J.A., Structured least squares to improve the performance of ESPRIT-type high-resolution techniques, in *Proc. IEEE Int. Conf. Acoust., Speech, Signal Processing,* V, 2805–2808, Atlanta, GA, May 1996.

[9] Haardt, M., Zoltowski, M.D., Mathews, C.P. and Nossek, J.A., 2D Unitary ESPRIT for efficient 2D parameter estimation, in *Proc. IEEE Int. Conf. Acoust., Speech, Signal Processing,* 3, 2096–2099, Detroit, MI, May 1995.

[10] Lee, A., Centrohermitian and skew-centrohermitian matrices, *Linear Algebra and its Applications*, 29, 205–210, 1980.

[11] Lee, H.B. and Wengrovitz, M.S., Resolution threshold of beamspace MUSIC for two closely spaced emitters, *IEEE Trans. Acoust., Speech, Signal Processing*, ASSP-38, 1545–1559, Sept. 1990.

[12] Linebarger, D.A., DeGroat, R.D. and Dowling, E.M., Efficient direction finding methods employing forward/backward averaging, *IEEE Trans. Signal Processing,* 42, 2136–2145, Aug. 1994.

[13] Mathews, C.P., Haardt, M. and Zoltowski, M.D., Implementation and performance analysis of 2D DFT Beamspace ESPRIT, in *Proc. 29th Asilomar Conf. on Signals, Systems, and Computers*, 1, 726–730, Pacific Grove, CA, Nov. 1995, IEEE Computer Society Press.

[14] Mathews, C.P., Haardt, M. and Zoltowski, M.D., Performance analysis of closed-form, ESPRIT based 2-D angle estimator for rectangular arrays, *IEEE Signal Processing Letters*, 3, 124–126, Apr. 1996.

[15] Mathews, C.P. and Zoltowski, M.D., Eigenstructure techniques for 2-D angle estimation with uniform circular arrays, *IEEE Trans. Signal Processing*, 42, 2395–2407, Sept. 1994.

[16] Mathews, C.P. and Zoltowski, M.D., Performance analysis of the UCA-ESPRIT algorithm for circular ring arrays, *IEEE Trans. Signal Processing,* 42, 2535–2539, Sept. 1994.

[17] Mathews, C.P. and Zoltowski, M.D., Closed-form 2D angle estimation with circular arrays/apertures via phase mode exitation and ESPRIT, in *Advances in Spectrum Analysis and Array Processing,* Haykin, S., Ed., vol. III, 171–218, Prentice-Hall, Englewood Cliffs, NJ, 1995.

[18] Roy, R. and Kailath, T., ESPRIT — Estimation of signal parameters via rotational invariance techniques, *IEEE Trans. Acoust., Speech, Signal Processing,* ASSP-37, 984–995, July 1989.

[19] Sensi, J., *Aspects of Modern Radar*, Artech House, 1988.

[20] Steinberg, B.D., Introduction to periodic array synthesis, *Principle of Aperture and Array System Design*, John Wiley & Sons, New York, chap. 6, 98–99, 1976.

[21] Swindlehurst, A.L. and Kailath, T., Azimuth/elevation direction finding using regular array geometries, *IEEE Trans. Aerospace and Electronic Systems*, 29, 145–156, Jan. 1993.

[22] Swindlehurst, A.L., Ottersten, B., Roy, R. and Kailath, T., Multiple invariance ESPRIT, *IEEE Trans. Signal Processing*, 40, 867–881, Apr. 1992.

[23] Xu, G., Roy, R.H. and Kailath, T., Detection of number of sources via exploitation of centro-symmetry property, *IEEE Trans. Signal Processing*, 42, 102–112, Jan. 1994.

[24] Zoltowski, M.D., Haardt, M. and Mathews, C.P., Closed-form 2D angle estimation with rectangular arrays in element space or beamspace via Unitary ESPRIT, *IEEE Trans. Signal Processing*, 44, 316–328, Feb. 1996.

[25] Zoltowski, M.D., Kautz, G.M. and Silverstein, S.D., Beamspace root-MUSIC, *IEEE Trans. Signal Processing*, 41, 344–364, Jan. 1993.

[26] Zoltowski, M.D. and Lee, T., Maximum likelihood based sensor array signal processing in the beamspace domain for low-angle radar tracking, *IEEE Trans. Signal Processing*, 39, 656–671, Mar. 1991.

[27] Zoltowski, M.D. and Stavrinides, D., Sensor array signal processing via a Procrustes rotations based eigenanalysis of the ESPRIT data pencil, *IEEE Trans. Acoust., Speech, Signal Processing*, ASSP-37, 832–861, June 1989.